

Dear Editor,

We appreciate the time and effort invested by both reviewers. In particular, we would like to thank Reviewer 1 for his or her kind words and thorough review, and we thank Reviewer 2 for raising valid and important questions about whether both our mooring arrays cover the entire extent of the plume and whether the overflow splits before arriving at section S so that the array might have missed one branch of the overflow. We respond to these concerns in detail in our revised Discussion section (see quotes below), including a new figure which shows the position of mooring array S in relation to earlier reported locations of the bifurcation. We are of the opinion that the addition of an in-depth discussion of the bifurcation location, and the other changes we have made following the reviewers' suggestions, have significantly improved our manuscript.

As pointed out by Reviewer 2, there was a discrepancy between Figure 3 and the values cited in the text. During the revision process, we found that the figure in question had been made erroneously using an older version of the post-processed data set, and that there was an inconsistency in the 'percent good' threshold used. In the final version of the manuscript, we ensure that all the figures, cited numbers and calculations consistently use the most recent version of post-processing and cut-off limits.

Here follows a point-by-point reply to the reviewers' comments, marked by "C". Our replies are marked by "R". At the end of the response letter, an annotated version of the manuscript shows all the changes made in detail.

## **Response to Reviewer #1.**

### SPECIFIC COMMENTS

C. 2316-18: "mean diffusivities" - probably "time mean vertical diffusivities"?

R. We changed this to "time mean vertical diffusivities".

C. 2316-22ff: If you want to describe the whole GSR overflow you also need to mention the IFR and WTR overflows.

R. We now mention the IFR and WTR overflows in the first paragraph of the Introduction: "Cold waters that flow from intermediate levels in the Nordic Seas into the North Atlantic must cross the shallow Greenland–Scotland Ridge. Overflows occur both across the Iceland–Faroe Ridge and the Wyville Thomson Ridge, but the densest overflow plumes are those passing through the deepest gaps in the Greenland–Scotland Ridge, namely the Denmark Strait and the Faroese Channels (Hansen and Østerhus, 2000; Saunders, 2001)."

C. 2317-1: Maybe more precise to say "the thermohaline composition of North Atlantic Deep Water"

R. We have changed this as suggested.

C. 2317-22: "similar results" - please specify results

R. We now specify (1) that the temperature thresholds gives similar values of height and width of the overflow plume as the other method, and (2) that the volume transport determined in this way, 1.6 Sv, agrees well with that of Hansen and Østerhus.

C. 2317-23: It would be helpful to mention instruments and averaging time span for the Hansen and Østerhus volume transport.

R. We now mention that the Hansen and Østerhus volume transport estimate is based on 10-year measurements (1995-2005) from moored ADCPs and temperature sensors.

C. 2319-5f: Continued moored measurements in the FBC since 95! This is one of the few global long term moored time series of (part) of the deep MOC, so I wouldn't say most of the work on the FBC has been based on hydrographic sections.

R. We have rewritten this paragraph to highlight the importance of the long-term time series from the FBC sill mooring: "The overflow transport is continuously monitored by moored instruments at the sill section, where at least one upward-looking ADCP mooring in the centre of the channel has been maintained since 1995 (see Hansen and Østerhus, 2007). Other work on the FBC overflow has often been based on hydrographic sections, sometimes combined with current measurements. Some studies have used e.g. short-term moorings (Dooley and Meincke, 1981) or gliders (Beaird et al., 2013).

Aside from the FBC sill mooring (Hansen and Østerhus, 2007), which provides one of the world's few long-term moored time series of a deep branch of the meridional overturning circulation, mooring measurements of the FBC overflow of more than a few months' duration are rare (e.g. Saunders, 1990; Darelius et al., 2011). In particular, few long-term observations have been made downstream of the sill, and none of them cover the whole vertical and lateral extent of the plume."

C. 2323-22: Do uncertainties become too large when going beyond January 17 with less instruments? My earlier understanding was that some ADCPs stopped sampling after about 3 months, so this statement doesn't make sense.

R. Three high-frequency ADCPs (one at C2, one at M1, and one at S3) were deployed to study mixing processes at the plume interface, and stopped sampling after 3 months because they were set to sample at a higher temporal resolution. Their stopping early was planned and did not affect the total vertical range of velocity measurements at those moorings. In our mooring design, we made sure to cover the same depth range using lower frequency ADCPs sampling for the entire duration of the deployment. However, the only ADCP at mooring C3 stopped recording (unplanned) after 234 days, and no vertical velocity profiles are available from that mooring after 17 January. One might attempt to construct full-depth velocities from C3 based on point measurements from the RCM-7 at 25 mab or using a relationship with velocities at C2, but considering that C3 has the highest velocities in the C-array we think that "making up" velocity records here would introduce an undesirable level of uncertainty in the transport estimates. We prefer to report volume transports only for the period during which we have velocity profiles from the ADCP at C3. This is now explained in appendix B.

We have also changed these lines (originally 2323-22) to specify that we are considering the period with "complete vertical coverage of velocity of the cold overflow plume at all C-array moorings", with a reference to appendix B.

C. 2323-24: How do you calculate the standard deviation of daily values?

R. As described (and cross-referenced to) in Appendix B, transport time series at each section were calculated using daily gridded fields. The standard deviation for each section is calculated over this daily time series. We have rephrased this to "standard deviation of the daily resolution time series".

C. 2325-5: Any idea what could cause a seasonal cycle in core plume temperatures? Hansen & Osterhus (2007) show a seasonal cycle in temperature with a minimum in July/August.

Hansen and Østerhus 2007 suggest that the seasonality in temperature is linked to the seasonality in volume flux: large outflow would draw the water from deeper depth and that would give lower temperatures. However, our volume transports do not show a clear seasonal cycle, probably because of

the limited record length – as discussed in our revised Discussion section: “Saunders (1990) found no seasonality of plume thickness, temperature or velocity in year-long measurements, but Hansen and Østerhus (2007) showed a seasonal variation of kinematic overflow at the sill of about 10% of the mean over a 10-year period. The relatively low amplitude of the seasonal cycle compared to shorter-term variations means it only becomes apparent in data sets covering several years. The seasonal variability in the outflow has been linked to seasonality in the barotropic northward flow of Atlantic Water in the Faroe--Shetland Channel (Lake and Lundberg, 2006). Darelius et al. (2015) showed that variability in volume flux on shorter time scales is linked to the local barotropic forcing.”

C. 2325-14: How do you know about semidiurnal variability in volume transport if daily averages were calculated? Why not calculate hourly transport and show the tidal peaks in the spectra?

R. This phrase about the tidal band variability is a remnant from our earlier calculations when we used hourly transports. We now remove this statement. There is indeed tidal variability, but this is not important for the focus of the present study. In our earlier analysis we used hourly fields, but then decided for using daily averages, mainly to remove the tidal variability. We retain this presentation.

C.2325-15: What is the difference between plume transport and total transport?

R. This initially referred to transport of overflow water and including modified overflow water, respectively, but since the maxima and minima of both occur in the same months we have changed this sentence to refer simply to "volume transport".

C.2325-9: Either swap Figs. 7 and 8 or mention Fig. 7 already when talking about volume transports in Section 4. I'd prefer the latter.

R. We amended the following in Section 4, first paragraph, with cross-reference to Fig 7: “Time series of daily transport across sections C and S are shown in Fig 7.”

C. 2328-18ff: The heat budget section needs a little more scrutiny. For the heat budget to work you need to assume steady state, this needs to be discussed. I do not understand the averaging process, what do you mean by "daily averaged data in 30 day windows to sufficiently average over the 3-5 day mesoscale variability"? Equations 1-4 need to express that quantities are averaged. Shouldn't the horizontal eddy temperature fluxes enter equations 3 and 4? What are the errors on volume transports Q3 and Q6 through upper isotherms?

R. We now mention that a steady state is assumed and also cite key references (Hogg et al., 1982, Whitehead and Worthington, 1982) which introduced the method and which also discuss various points raised by the reviewer. The budget equations are solved using 30-day averaged parameters (Q, T, etc.) which are daily data. The calculations are done using 30-day width windows which are moved by 1-day. That is at each day we have output from the budget calculation. The 30-day window is long enough to average over several 3-5 day scale oscillations. We clarified these points in the revised version using: “The budget was calculated using averages over 30-day long segments of the daily time series which are moved by 1 day throughout the record (that is, 1-day moving 30-day width windows). The 30-day window sufficiently averages over the 3-5 day mesoscale variability. While the steady-state assumption is questionable, the variability in section volume transports is mainly contained in time scales less than 10 days (see Fig. 10 for the variance-preserving transport spectra). Budget calculations using time average windows from 5 days to 3 months with 5-day increments (not shown) confirm that the results are not sensitive to the choice of the 30-day window after approximately 15-25 days. We thus expect the budget calculations to be fairly representative of the steady state, and to yield a more accurate estimate of entrainment rates compared to analysis of snapshots of hydrography and currents from single

cruises.”

We now express in Eq 1-4 that we are using averaged quantities. Under Eq 2, we amended:

“... (array S), and all quantities are time averaged over a suitable time window...”

Here it suffices to mention a suitable window, because in the next paragraph we justify the choice of 30 day.

We repeated the budget calculations using time average windows from 5 days to 3 months with 5-day increments. These calculations (not shown) confirm that the results are not sensitive to the choice of the 30-day window after approximately 15-25 days.

Q3 is solved as the residual of Eq(1) and is bounded by the upper layer. The only uncertainties are thus those associated with the volume flux measurements at Sections C and S, and with the bottom Ekman transport. The drag coefficient used in the Ekman transport is from turbulence measurements and, on average, is well constrained. Q6 is the residual of Eq(2) after Q3 is obtained. Error in Q3 is thus carried over to Q6.

C. 2329-10: The equation relating turbulent vertical heat flux is defined locally, not in an area-averaged sense as implied here. The quantity you get from the heat budget, averaged over the volume/area defined by the mooring arrays, is the heat flux. Calculating an average vertical diffusivity can be misleading as  $K$  and  $dT/dz$  may not be independent from each other.

R. Agreed. We clarified this point under Eq.(4), by revising as:

“..The diffusive heat flux, averaged over volume and time, is approximated as  $F_H = -K_z (dT/dz) L W$ , where  $K_z$  is the average vertical diffusivity,  $L$  is the horizontal along-path separation between the arrays,  $W$  is the average plume width defined by the given isotherm, and  $dT/dz$  is the average vertical temperature gradient. This approximation is typically invoked in the budget calculations, and is valid if the local values of diffusivity and the vertical temperature gradient are not correlated. Our resulting estimates of average vertical diffusivity should thus be interpreted with this caveat in mind.”

C. 2329-26: I am not convinced yet that the Ekman transport can be neglected in the heat budget. The plume has lateral temperature gradients as you move from the edge to the center, i.e. the zero degree core of the plume doesn't cover its whole width. Also, at Section S there is no zero degree water left. You mention transverse circulation later in the discussion (2332-23), could this not be at play here?

R: The part of the control volume emanating from the channel is constrained within the channel such that the bottom Ekman transport is retained within the plume. The export only happens on the open slope. Given an estimate of 0.3 Sv for  $Q_{EK}$ , and  $T$  close to nil (say as large as 1°C), the term  $Q_{EK}T_{bottom}$  is very small compared to the other advective temperature flux terms. The possible effect of transverse circulation should be included in the estimated average entrainment/detrainment results.

C. 2330-7:  $K$  is usually termed vertical diffusivity, not eddy diffusivity.

R. Agreed. We replaced eddy diffusivity with vertical diffusivity throughout.

C.2333-1: What could be the important implications?

R. We now mention the implications in the Discussion section: “Simple estimates of the contribution of the FBC overflow to the global thermohaline circulation assume doubling of the volume transport due to entrainment. Our observations suggest that despite substantial entrainment, volume transport does not increase significantly because of detrainment, implying that the impact of FBC overflow on the global thermohaline circulation can be less than what has usually been assumed.”

C.2333-18: Again, K should be vertical diffusivity.

R. Changed to "vertical diffusivity".

C.2334-7: Great to see that horizontal eddy fluxes are consistent with baroclinic instabilities generating the eddies!

R. We agree.

C.2335-12: Repeating the heat budget results here seems a little out of place where one expects a more general closing statement.

R. Agreed. We move the inferred mean vertical diffusivities 3 sentences up, before "The present study provides...", and improved our final paragraph so that it now mentions the important implications discussed above. Our new closing paragraph reads: "The contribution of the FBC overflow (and the dense Greenland--Scotland Ridge overflows in general) to the North Atlantic Deep Water is sometimes estimated based on an assumed doubling of the volume transport due to a factor of two entrainment. Our data, although limited to a region close to the overflow site, suggest that this is not accurate. As the plume proceeds into the stratified ambient water, there is substantial detrainment from the deeper layer, of comparable magnitude to the entrainment into the interfacial layer. A simplified view of along-path entrainment of a gravity current is thus not valid for the FBC overflow. A more accurate quantification of the FBC overflow on the global thermohaline circulation merits further studies"

C.2336-4: Table A2 does not list the percentage of data discarded.

R. We now include the percentage of data discarded in the table.

C.2336-10: Does it make a difference if you calculate volume transport from hourly observations of T and v and then low pass-filter? Why do you reduce your resolution in time?

R. As mentioned above, since the higher (i.e. tidal) frequencies are not the focus of this study, we decided to use daily averages. However, we have also calculated volume transports based on hourly fields; the results of low-pass filtering these are not significantly different from those computed using daily fields.

C.2337-1: Would it make a difference if all velocities were included?

R: No. We use this criterion because we define overflow as transport out of the FBC toward the North Atlantic only. This is the dominant mode of transport, and including reverse velocities makes no significant difference.

C. Figure 1: Labels on the depth contours would be helpful. Also, colorbar should be labeled here and elsewhere.

R. We have labelled depth contours in Fig. 1. We have also labelled the colorbar in this and all other figures with colorbars.

C. Figure 4: Different colormaps for time-mean and standard deviation would make this figure much easier to interpret. Again, colorbars should have labels.

R. We have changed the colour map for standard deviation so that it is different to that of the mean. As mentioned above, we have labelled all the colorbars throughout the manuscript.

## TECHNICAL CORRECTIONS

C. 2316-5 arrays were deployed - use past here and elsewhere if applicable  
R. We have changed to past tense in the abstract.

C. 2319-22: at section C, at section S  
R. Changed.

## Response to Reviewer #2.

C. The results presented are very important for our understanding of the role of Faroe Bank Channel (FBC) overflow in the global thermohaline circulation. In the simplest picture, FBC-overflow provides  $\approx 2$  Sv of  $\approx 0^\circ\text{C}$  water, which entrains ambient waters of  $\approx 6^\circ\text{C}$  so that the total contribution to NADW is  $\approx 3^\circ\text{C}$ . This implies that the overflow entrains similar amounts of ambient waters. Thus, if there is no detrainment, as claimed by Mauritzen (2005), then FBC-overflow should supply 3-4 Sv of overflow + entrained water to NADW. From the  $\approx 1\text{-}2^\circ\text{C}$  warming of bottom water in Geyer et al. (2006), most of this entrainment should also have occurred before the downstream array (the S array) in the present study. Although this calculation is very much simplified and probably is an overestimate, we would have expected more than 2 Sv of water  $< 3^\circ\text{C}$  through the downstream array (S array). But, Ullgren et al. report only 0.8 Sv. Instead of considerable volume transport increase due to entrainment, volume transport is substantially decreased due to detrainment. If these claims are supported, the impact of FBC-overflow on the THC is much less than what has usually been assumed. Unfortunately, I am not convinced that this is the only way to interpret the observational results, because they are based on an assumption that is not well justified in the manuscript. This assumption is that both mooring arrays (sections) cover the entire overflow plume. For the upstream array (C section), this is probably fairly correct although Figure 4 clearly shows overflow water to the left of (south of) mooring C3. For the downstream array (S section), this assumption is less convincing. This section is on the slope (Figure 2) and the moorings do not cover the deepest part of the channel. Thus, there is a priori no guarantee that the array covers the whole overflow plume, but the authors claim this (p.2319, l. 8-10 and p. 2335, l. 8-9). I have not found any arguments, on which they base this claim, but I assume that the main reason is the weak flow at S4.

R. The reviewer raises a valid concern. We now address the question about whether both mooring arrays cover the entire plume in the discussion section as follows:

“Our data set, however, shows no corresponding increase from mooring array C to array S. To explore this surprising result, we must first ask ourselves whether our measurements covered the entire plume at both sections.

At array C, overflow water on average occupied the lower 120 m at the southernmost mooring (see section 3). The southern boundary of the plume must thus be south of the mooring section, but because the flow here is constrained by topography the plume cannot extend far to the south. Our horizontal extrapolation adequately compensates for the edges of the plume; our mean volume transport estimate for water colder than  $3^\circ\text{C}$  of  $1.3 \pm 0.3$  Sv is within the range of earlier estimates for the FBC overflow varying between 1.1 and 2.1 Sv (van Aken and Becker, 1996; Hansen and Østerhus, 2000; Kanzow and Zenk, 2014). The estimated volume transport at array C is about 2/3 of the kinematic overflow estimate at the sill (Darelius et al., 2015, and Appendix B).

The S section was not located in the channel, but on the open slope. The question of how that mooring array was positioned with respect to the plume path is therefore important. First, we consider the statistics of the observed temperature and velocity at the moorings at section S. There was a clear presence of overflow water throughout the year at the two moorings S2 and S3 in the centre of the array, while at the two moorings at the edges, cold plume waters were only occasionally present. At the northernmost mooring, S1, overflow waters ( $T \leq 3^{\circ}\text{C}$ ) were found at 80 mab (the only measurement level here) less than 10% of the time and modified overflow waters ( $T \leq 6^{\circ}\text{C}$ ) less than 35% of the time. At the southernmost mooring, S4, the corresponding percentages at the same height above seabed were less than 2% for  $T \leq 3^{\circ}\text{C}$  and about 36% for  $\leq 6^{\circ}\text{C}$ . At both moorings, the lowest temperatures were correlated with stronger along-stream velocity, a clear indication of plume presence at such occasions. Cold water was present at these moorings only during periods with energetic oscillations (Darelius et al., 2015), suggesting that it is brought here by the eddy motion. Most of the time, however, the overflow was found in the centre of the array while absent at the outer moorings (i.e. the boundaries of the plume were found within the mooring array).

While there are no channel walls here to contain the overflow, the shallow topography north of array S likely prevents large excursions of the plume to the north (upslope). There is no evidence in literature of a plume path north of mooring S1. The mean current of the overflow mainly follows isobaths (Geyer et al., 2006), until it begins to descend under the influence of friction (Seim et al., 2010). Are there then downslope excursions that make the overflow pass south of section S? As mentioned above, the occurrence of cold water at mooring S4 was rare, and the long-term average velocity there was approximately zero (see figures 1 and 3). Our observations thus do not show any evidence of significant overflow at (or beyond) the southern end of array S.

C. From Geyer's (2006) Figure 3, we know, however, that the overflow plume splits into (at least) two separate branches. If the splitting occurs before the S array, then the weak flow at S4 could be because this mooring was located between the branches and the S array would not cover the whole of the overflow plume. The authors of the present manuscript are well aware of this branching (p.2317, l. 13-16), but they are apparently convinced that it occurs after their S array. That may perhaps be the case, but in view of the high-impact results presented, this has to be better justified. I have not been able to find observational evidence to support or reject this assumption conclusively, but Mauritzen et al. (2005) have a section (G section), which seems to run very close to the S array of Ullgren et al. On that section, Mauritzen et al. found overflow water below 1000 m depth (their Figures 23 and 24) and even two XCP profiles with bottom depths > 1000 m and core velocities exceeding 1 m/s (their Figure 25). Thus, it is not obvious to me that the basic assumption in this manuscript is valid. In conclusion, Ullgren et al. need either to present more convincing evidence that their assumption is valid, or modify the analysis and results of the manuscript accordingly.

R. We thank the reviewer for bringing up this important question. We are indeed aware of the bifurcation but as the reviewer suggests, we believe that it most likely occurs west (downstream) of the S array. We have now added several paragraphs to the Discussion section (see below) where we explain our reasoning, and added a new map (new Fig. 17) showing the location of our moorings along with those of observations in several other papers. In addition to the revised text of the manuscript, we would like to reply to some of the specific points raised by the reviewer as follows: Mauritzen et al. (2005) mention that the first occupation of section G, shown in their Figures 23 and 24, took place during a storm that was severe enough that operations temporarily had to be suspended, and they note that volume transport doubled after the storm (although it is uncertain whether this is directly

linked to the storm). For Mauritzen's figure 25, showing XCP profiles with high velocities at depths >1000 m, only the profiles with the highest velocities were shown. The profiles down to just under 1100 m are similar in depth to mooring S4, where high velocities were also observed, but only rarely and seemingly associated with eddy activity (cf. Darelius et al., 2015). Our year-long measurements from several moorings, in combinations with several repeats of the co-located CTD section (see Ullgren et al., 2014, referred to in the revised Discussion text) complement Mauritzen's two occupations of CTD section G, and -- given the high temporal variability in the region -- significantly improves the picture. Mauritzen et al. write (p. 910): "Between section G and the final section H the plume cannot sink further, and it decelerates. It also appears to separate into two paths, separated by a plateau in the topography." We agree with them on where the splitting occurs, namely after their section G (and thus after our section S); the plateau in question is most likely the one labelled in our new Fig. 17. Mauritzen et al. (2005) further write that "Such a splitting of the plume is also known from historical data." The historical data in question are not specified in their 2005 paper, but after studying reports from e.g. the Overflow 1960 and Overflow '73 expeditions, we are convinced that most evidence points towards a likely splitting of the flow a short distance downstream of our mooring array S -- as outlined in the revised Discussion, where we write:

"A second important issue to consider is the bifurcation of the flow. The overflow is known to split into two branches. The shallower branch flows westward, approximately following the isobaths along the Atlantic flank of the Iceland-Faroe Ridge, and the deeper branch turns southwestward, and descends more directly into the southern Iceland Basin (Beaird et al., 2013; Hansen and Østerhus, 2000). The splitting appears to occur between the secondary sill at about 9°W and a topographic "bump" or plateau further downstream (Mauritzen et al., 2005; Beaird et al., 2012, 2013). In designing our mooring array S, we chose a location to the east (i.e., upstream relative to the overflow) of the suspected bifurcation location to ensure an as complete as possible lateral coverage of the plume. Could the weak flow at mooring S4 indicate that the bifurcation occurred upstream of array S and that S4 thus was located between the branches? We turn to literature to find out where this bifurcation is most likely to occur. Repeat hydrographic sections from the multi-vessel "Overflow" survey in June 1960 (Lee, 1967; Tait, 1967) showed the cold core of the overflow centred at about 800 m depth, 10°W (station F1 at 61°54'N, 10°06'W -- very close to the 'bump' centred at 61°54'N, 10°07'W; cf. Beaird et al., 2012). However, maps of overflow thickness and percentage overflow water based on the same survey data suggested a bifurcation of the overflow beginning already upstream of this (see figures 3:108 and 3:109 in Hermann, 1967). Synthesizing the observations of the 1960 survey, the "Overflow 1973" experiment (Müller et al., 1979), and some evidence from geological studies, Hansen and Østerhus (2000) suggested an "alternative path" (see their fig. 43 and 49) for the overflow, turning southwestward and descending more directly and deeper in the (south-eastern) Iceland Basin. In a more recent study, the bottom temperature distribution measured by gliders indicated a branch of the overflow descending deeper than 1000 m, somewhere in the region close to our mooring section S (purple line in fig. 17; cf. Beaird et al., 2013). This branch appeared to the west of our array S, and could not be resolved because of 1000-m depth rating of the gliders.

During a survey conducted in June 2000, Mauritzen et al. (2005) found dense waters and high velocities as deep as between the 1000 and 1200 m isobaths at their section G, only about 5 km downstream of our array S (fig. 17, for comparison, mooring S4 was located at a depth of 1082 m). The authors remark, however, that the occupation of section G shown in the paper (their figures 23 and 24) took place after a storm when the overflow transport doubled. A better temporal averaging is provided from the survey in June 2012 reported in Ullgren et al. (2014). In a section repeated five times over the course of 70 h, located about 10 km upstream of our mooring array S, the high-velocity core of the overflow was mostly

centered close to, or shallower than, the 1000-m isobath, with reduced flow at the outer two stations (Ullgren et al., 2014).

Mauritzen et al. (2005) mention that a division into two branches at about 900 m depth is indicated at their westernmost section, H, located about 50 km downstream of our array S. (Section H is marked by green dots but not labelled in figure 17; it is the section the lower part of which is parallel and close to Geyer's section A.) They suggest that the bifurcation occurs somewhere between their sections G and H, where the flow decelerates and is "separated by a plateau in the topography" (Mauritzen et al., 2005, , p. 910). Most likely this flow separation is thus caused by the same topographic feature as Beard et al. (2013) refer to as the 'bump' (see fig. 17).

Mean current velocity vectors from July–November 1999 presented by Geyer et al. (2006) show a split into two branches at about 11°W (their Fig. 3), also west of our mooring section S (see Fig. 17). Note that this is a split of a deeper flow around a different topographic feature, southwest of the bump of Beard et al. (2013). The location of the knoll dividing the flow in the paper by Geyer et al. (2006) fits with the observation by Swift (1984) that data sets from the Overflow 1960 and 1973 expeditions (Tait, 1967; Müller et al. , 1979) both show a "similar three-way splitting of the overflow tongue at about 61°45'N and 11°W".

The complex topography that varies strongly on small scales is a major factor controlling overflow pathways in simulations (Chang et al., 2009). Tracer-weighted average plume paths from model experiments by Seim et al. (2010) and Riemenschneider and Legg (2007) generally turn more southward and descend below the 1000 m isobath close to (but typically west of) the location of array S.

Further evidence of the overflow splitting into a deeper and a shallower branch in the region just west of array S is found in velocities measured at 64 mab by a deep towed vehicle (Fig. 7 in Duncan et al., 2003). The current below about 900 m veered downslope at a section located about 20 km downstream of array S (Fig. 17). Two out of the three bottom-following float trajectories shown by Prater and Rossby (2005) followed roughly along the 1000-m isobath until at least 11°W, while one track descended earlier (closer to mooring array S). It should be noted that for the latter, as well as for one of the other floats, the positions along this part of the track were only estimates, not directly determined by sound ranging. We conclude that while the mooring array S is located in the region where the FBC overflow divides into two branches, a detailed comparison with earlier work suggests that the split takes place downstream of array S. We are reasonably confident that mooring array S did not miss a branch of the overflow because the bifurcation (or *one* bifurcation) is most likely caused by the topographic bump centred at about 61°54'N, 10°07'W, approximately 30 km downstream of array S. The deeper branch of the overflow and its path into the Iceland Basin merit further studies."

#### DETAILS

C. 1) In the first line of the abstract, it says ten moorings. In the first line of Part 2, it says nine moorings. In Table A1 and the paper as a whole, there are 8 moorings.

R. Corrected. It now says eight moorings in the abstract and in text throughout.

C. 2) On p. 2322, l.21-22, it says that time-average u-velocity reaches 94 cm/s at mooring S3, but that is not what you see on Figure 3c.

R. Figure 3c was by mistake made using an older version of the processed data set, and there was an inconsistency in the cut-off threshold for percent good data for the figure and the cited numbers. This has now been corrected. The correct time-average u velocity is 90 cm/s and this is also shown in the updated figure.

C. 3) P. 2326, l. 27: Should "S2" here be "S3" ?

R. Yes, thanks for noticing. This has been corrected.

C. 4) Caption for Figure 12: Have colours been swapped?

R. Yes, the colours were the wrong way around in the caption – this has now been rectified.

C. 5) Caption for Figure 12, first line: "aray" -> "array"

R. Corrected.

C. 6) Caption for Figure 13, last line: "for for" -> "for"

R. Corrected.

Manuscript prepared for Ocean Sci. Discuss.  
with version 2015/04/24 7.83 Copernicus papers of the L<sup>A</sup>T<sub>E</sub>X class copernicus.cls.  
Date: 13 January 2016

# Volume transport and mixing of the Faroe Bank Channel overflow from one year of moored measurements

J. E. Ullgren<sup>1</sup>, E. Darelius<sup>2</sup>, and I. Fer<sup>2</sup>

<sup>1</sup>Nansen Environmental and Remote Sensing Center, Bergen, Norway

<sup>2</sup>Geophysical Institute, University of Bergen and Bjerknes Centre for Climate Research, Bergen, Norway

Correspondence to: I. Fer (ilker.fer@uib.no)

## Abstract

One-year long time series of current velocity and temperature from ~~ten~~ eight moorings deployed in the Faroe Bank Channel (FBC) are analysed to describe the structure and variability of the dense overflow plume on daily to seasonal time scales. Mooring arrays ~~are~~ were deployed in two sections: located 25 km downstream of the main sill, in the channel that geographically confines the overflow plume at both edges (section C), and 60 km further downstream, over the slope (section S). At section C, the average volume transport of overflow waters ( $< 3^{\circ}\text{C}$ ) from the Nordic Seas towards the Iceland Basin ~~is~~ was  $1.3 \pm 0.3$  Sv; at Section S, transport of modified overflow water ( $< 6^{\circ}\text{C}$ ) ~~is~~ was  $1.7 \pm 0.7$  Sv. The volume transport through the slope section ~~is~~ was dominated by mesoscale variability at 3–5 day time ~~scales~~ scales. A simplified view of along-path entrainment of a gravity current ~~is not~~ appears not to be accurate for the FBC overflow. As the plume proceeds into the stratified ambient water, there is substantial detrainment from the deeper layer (bounded by the  $3^{\circ}\text{C}$  isotherm), of comparable magnitude to the entrainment into the interfacial layer (between the 3 and  $6^{\circ}\text{C}$  isotherms). ~~Time~~ A time series of gradient Richardson number suggests a quiescent plume core capped by turbulent near bottom and interfacial layers in the channel. At section S, in contrast, the entire overflow plume is turbulent. Based on a two-layer heat budget constructed for the overflow, ~~mean time~~ mean vertical diffusivities at the top of the bottom layer, and across the interfacial layer ~~are~~ were  $(30 \pm 15) \times 10^{-4} \text{ m}^2 \text{ s}^{-1}$  and  ~~$(119 \pm 43) \times 10^{-4}$~~   $(120 \pm 43) \times 10^{-4}$   $\text{m}^2 \text{ s}^{-1}$ , respectively.

## 1 Introduction

~~Gold waters~~ Cold waters that flow from intermediate levels in the Nordic Seas ~~flow into the North Atlantic must cross the shallow Greenland–Scotland Ridge. Overflows occur both across the Iceland–Faroe Ridge and the Wyville Thomson Ridge, but the densest overflow plumes are those passing~~ through the deepest gaps in the ~~shallow Greenland–Scotland ridge, Greenland–Scotland Ridge, namely~~ the Denmark Strait

and the Faroese Channels, and enter the North Atlantic as dense overflow plumes (Hansen and Østerhus, 2000; Saunders, 2001) (Hansen and Østerhus, 2000; Saunders, 2001). The water mass transformation that occurs as the overflows mix with the overlying Atlantic waters plays an important role in determining the thermohaline composition of the North Atlantic North Atlantic Deep Water (Dickson and Brown, 1994; van Aken, 2007). Here, we report on measurements of the overflow from the Faroe Bank Channel (FBC).

The FBC is a narrow channel with steep side walls (Fig. 1). The primary sill, where the channel is at its narrowest and shallowest, is about 15 km wide and 840 m deep. Approximately 95 km northwest of the sill, where the channel is wider and the sides less steep, there is a second sill of about 850 m depth (Beaird et al., 2012). The overflow from the Nordic Seas enters the FBC from the Faroe–Shetland Channel to in the east and flows through the channel towards the northwest; we use “upstream” and “downstream” hereafter in the sense of the plume flow. The overflow takes the form of a well-mixed bottom layer, overlaid by a stratified interfacial layer (Fer et al., 2010). After passing through the channel, the flow widens from about 10 km at the primary sill to about 30–40 km on the slope after the secondary sill (Duncan et al., 2003; Beaird et al., 2013). Beyond this point, the flow splits into two branches: a deep one that reaches depths exceeding 1000 m, containing the densest part of the plume and about 2/3 of the total volume transport, and a shallower branch along the slope of the Iceland–Faroe Ridge at intermediate depths (Beaird et al., 2013).

The waters feeding the overflow are composed of cold, low-salinity water masses, Norwegian Sea Deep Water and Norwegian Sea Arctic Intermediate Water, both with temperatures close to or below 0 °C (e.g. Hansen and Østerhus, 2000; Fogelqvist et al., 2003). Near the sill, the overflow is typically defined as water colder than 3 °C (e.g. Borenäs and Lundberg, 1988; Hansen and Østerhus, 2007). This temperature threshold gives similar results values of height and width of the overflow plume as selecting the quasi well-mixed bottom layer from temperature or salinity profiles (Duncan et al., 2003). Hansen and Østerhus (2007) estimated the The resulting estimate of volume transport of water colder than 3°C at the sill to 1.71.6 Sv (1 Sv  $\equiv$  10<sup>6</sup> m<sup>3</sup> s<sup>-1</sup>) computed from shipboard

observations (Duncan et al., 2003) agrees very well with the 10-year average for the period 1995–2005 of 1.7 Sv based on moored acoustic Doppler current profilers (ADCPs) and temperature sensors (Hansen and Østerhus, 2007).

Along its path through the FBC, the plume entrains the overlying warmer and more saline Atlantic Water, and attains higher temperatures downstream (Saunders, 1990; Mauritzen et al., 2005). Upon exiting the Channel, the plume also encounters low-salinity, low-oxygen Intermediate Water from the Iceland Basin which mixes into the interfacial layer above the plume and contributes to the water mass mixture from the FBC that eventually forms a part of the North Atlantic Deep Water (Ullgren et al., 2014).

The overflow through the channel is energetic, with a long-term average velocity at the sill of up to  $120 \text{ cm s}^{-1}$  (Hansen and Østerhus, 2007). The plume accelerates as it descends along the deepening topography, and maximum overflow velocity is found downstream of the sill (close to  $9^\circ \text{ W}$ ; Fer et al., 2010). The swift flow is associated with high levels of turbulence, and a region of intense mixing (e.g. Fer et al., 2010). The secondary sill, where the plume thins significantly, is observed to be the most significant location in terms of mixing and water mass transformation (Beird et al., 2012, 2013).

Currents and temperatures in the region downstream of the sill vary strongly on time scales of a few days (Geyer et al., 2006), reflected in high variability of the sea surface height field (Høyer and Quadfasel, 2001). The dense overflow takes the form of a train of 100–200 m thick boluses of cold water moving along the slope at periods of 2.5–6 days (Darelius et al., 2011). The cold water domes are associated with energetic mesoscale oscillations in the velocity field, that extend throughout the water column, and are linked to a wave pattern in sea surface height (Darelius et al., 2013). Guo et al. (2014) propose that these mesoscale eddies are caused by baroclinic instabilities of the overflow plume.

Because of its important role in large-scale circulation, carrying one third of the total volume of dense overflows from the Nordic Seas into the North Atlantic, the FBC overflow has garnered scientific interest for many decades. Hansen and Østerhus (2000) compiled a number of volume transport estimates for the FBC overflow from literature, and their summary was more recently reviewed and augmented by Kanzow and Zenk (2014).

Several other studies have dealt with aspects of the overflow such as friction and mixing (e.g. Duncan et al., 2003; Borenäs and Lundberg, 2004; Mauritzen et al., 2005; Fer et al., 2010), presenting additional transport estimates. ~~Most of the~~ The overflow transport is continuously monitored by moored instruments at the sill section, where at least one upward-looking ADCP mooring in the centre of the channel has been maintained since 1995 (see Hansen and Østerhus, 2007) . Other work on the FBC overflow has often been based on hydrographic sections, sometimes combined with current measurements; ~~some~~ . Some studies have used e.g. short-term moorings (Dooley and Meincke, 1981) or gliders (Beaird et al., 2013). ~~The overflow transport is monitored by moored instruments at the sill section, where at least one upward-looking ADCP mooring in the centre of the channel has been maintained since 1995 (see Hansen and Østerhus, 2007)~~ . Mooring ~~Aside from the FBC sill mooring (Hansen and Østerhus, 2007)~~ , which provides one of the world's few long-term moored time series of a deep branch of the meridional overturning circulation, mooring measurements of the FBC overflow of more than a few months' duration are rare (e.g. Saunders, 1990; Darelius et al., 2011); ~~in particular~~ . In particular, few long-term observations have been made downstream of the sill, and none of them cover the whole vertical and lateral extent of the plume.

This study is based on the first mooring measurements to cover the full width and height of the plume for a whole year, simultaneously by two arrays, one in the channel and a second one over the Iceland–Faroe slope. These mooring data were first presented by Darelius et al. (2015), who investigated variations in the strength and periodicity of mesoscale oscillations. In this paper we take a broader view and address mainly the mean hydrographic and velocity characteristics of the overflow plume, its stability, mixing, and transport.

## 2 Data and methods

Data were collected in the Faroe Bank Channel overflow region using ~~nine~~ eight bottom-anchored moorings, in the period between 28 May 2012 and 5 June 2013 (Fig. 1). The “Channel” (C) mooring array was located 25 km downstream of the sill in the FBC, and the

“Slope” (S) array a further 60 km west where the plume exits the narrow confines of the channel. Between the two sections, a single mooring, M1, was located 16 km upstream of section S along the main path of the plume. The horizontal separation between moorings was 7–8 km ~~on at~~ section C, and 10–12 km ~~on at~~ section S.

The moorings were equipped with temperature recorders (Sea-Bird Electronics, SBE39 and SBE56), conductivity-temperature-pressure recorders (SBE37, Microcats), Andraea current meters (RCM7/8), Nortek current meter (Aquadopp), and ~~acoustic Doppler current profilers (ADCPs, ADCPs)~~ (RD-Instruments 75/150/300 kHz Workhorse, Andraea 600 kHz RDCP and Nortek Continental). Instrumentation and location of the moorings are listed in Appendix A1, Table A1, and a schematic of the mooring array design is shown in Fig. 2. The sampling rate was 15 s for SBE56s, 5 min for SBE37s and SBE39s, 5–60 min for ADCPs, 1 h for RCMs, and 20 min for the Aquadopp. Three RDI 300 kHz ADCPs located at the core of the plume (at moorings C2, M1, and S3) and vertically positioned in the interfacial layer were set to sample for a shorter duration (3–4 months) at high resolution in time and in the vertical to study mixing processes, to be presented elsewhere. The high frequency ADCPs are included in mooring descriptions for completeness, however, they are excluded when generating the gridded fields (see below), because the vertical extent they ensonified were also covered by lower frequency ADCPs which recorded for the entire deployment. Here we report the hourly averaged data.

The coordinate system for each mooring is aligned with the orientation of the mooring section, so that the  $x$  axis is perpendicular to the section and the  $y$  axis parallel to the section, pointing upslope (see right inset in Fig. 1). The angle of rotation ( $\beta$ ) is  $34^\circ$  and  $31^\circ$  (clockwise, around the  $z$  axis) for the C and S arrays, respectively.

The position of an individual mooring element relative to the anchor varies with the current and drag on the mooring. Time series of the vertical position and tilt of the instruments were calculated using the measured currents (hourly mean values) and the software *Mooring Design and Dynamics* (MDD; Dewey, 1999), which calculates the behaviour of a mooring in a given, three dimensional sheared current by balancing the forces acting on the mooring. The results compared well with the available pressure measurements. Statistics and further

details regarding mooring pulldown and instrument tilt are given in Appendix A2. Hourly velocity and temperature records at corrected depths were then linearly interpolated to 1 m vertical resolution.

During the mooring deployment cruise on board R.V. *Håkon Mosby* between 26 May and 14 June 2012, a total of 146 CTD profiles were collected, see Ullgren et al. (2014). Cruise measurements were used to verify mooring temperature, salinity, and velocity data. The moored  $T - S$  data showed a tight relationship between temperature ( $T$ ) and potential density anomaly ( $\sigma_\theta$ ). Data from all moored  $T - S$  sensors were fitted to a third degree polynomial,  $\sigma_\theta = -(2.0 \times 10^{-4})T^3 - (2.0 \times 10^{-3})T^2 - (4.22 \times 10^{-2})T + 28.0505$   
 $\sigma_\theta = -(4.7 \times 10^{-4})T^3 + (4.9 \times 10^{-4})T^2 - (4.52 \times 10^{-2})T + 28.0536$  (root mean square error  $0.0130.034 \text{ kg m}^{-3}$ ). This allows density to be inferred from temperature measurements alone, which is desirable given the better coverage by the temperature sensors. The relation was not significantly different using monthly subsets of the data.

Temperature records are used to identify different layers in the water column. Following e.g., Hansen and Østerhus (2007); Mauritzen et al. (2005), we use the level of the  $3^\circ\text{C}$  isotherm as a delimiter of overflow water at array C. (Bottom water with temperature  $< 0.3^\circ\text{C}$  – the stricter definition of overflow used by Hansen et al., 2001 – will be referred to as very cold water.) The overflow water found further downstream is diluted by entrained warmer water; it will be referred to as modified overflow water, and delineated by the  $6^\circ\text{C}$  isotherm (cf. Darelus et al., 2015; Guo et al., 2014). The Atlantic Water of the upper layer is defined by a temperature of  $\geq 8^\circ\text{C}$ , while waters with temperature  $6^\circ\text{C} < T < 8^\circ\text{C}$  will be referred to as intermediate water.

Volume transports through the channel and slope sections were determined from velocity and temperature data as described in Appendix B and in Sect. 4.

### 3 Average conditions

#### 3.1 Thermal structure of the plume

The dense overflow plume was thicker and colder at the channel mooring section than at the downstream section (Figs. 3 and 4). The bottom layer at the southernmost mooring in array C (C3) was the coldest, with a mean temperature at ~~30~~26 m above bed (mab) of  $-0.3^{\circ}\text{C}$  over the one year deployment. However, although the very cold water occasionally reached up to ~~150~~140 mab (~~the top of the instrumentation~~) at mooring C3, it was mostly present only as a thin layer. Between 30 and 100 mab temperatures increased sharply where the bottom layer was capped by strong stratification. The overflow water was generally contained within the bottom 120 m.

In the centre of section C, at mooring C2, the plume was thicker. The presence of very cold water was not as frequent as at C3 – ~~less than only about~~ about 60 % of the time even at the deepest level – but overflow water on average occupied the lower 200 m of the water column (Fig. 3). Above about 50 mab, the mean temperature at mooring C2 was thus colder than at C3.

The northernmost mooring (C1) in array C was located outside the main path of the plume; very cold water occurred here only  $< 5\%$  of the time. When present, the overflow covered up to about 100 m from sea bed, ~~however, 25;~~ however, 30 % of the time no overflow was recorded.

At mooring array S, the plume was thinner and warmer than at C, even in the bottom layer. Very cold water occurred only occasionally in the deepest layer at the two central moorings S2 and S3. At S2, the plume water ( $T < 3^{\circ}\text{C}$ ) reached up to about ~~75~~60 mab, overlain by a ~~60~~40 m thick interfacial layer; ~~at~~ At S3, ~~both~~ the bottom and the interfacial layer were ~~even thinner~~ equally thin. Above the interfacial layer there was a 100–200 m layer of intermediate water, and Atlantic Water was found above about 200–300 mab. The water column structure at mooring S4, 14 km further south-west, was markedly different as this southernmost mooring in the S array was located outside the plume. Overflow water was measured only ~~2–3%~~ about 20% of the time at the deepest level, coinciding with eddy

activity, while intermediate water took up ~~most~~ a large part of the water column at S4, ~~sometimes~~ occasionally reaching the bottom.

### 3.2 Velocity characteristics

The mean current in the near-bottom layer was directed towards the north-northwest at section C and turned more towards the west-northwest at section S (Fig. 1). The average current was in this alongstream direction throughout the part of the water column occupied by the cold, dense plume and the interfacial layer.

The maximum plume velocity was found in the bottom 50 m at mooring array S, where the time-average velocity perpendicular to the mooring section ( $u$ , see Sect. 2) reached 9490  $\text{cm s}^{-1}$  (mooring S3; see Fig. 3). Similar but somewhat weaker velocities occurred at mooring C3. The thickness of the maximum velocity layer, in contrast, was significantly larger at the upstream array C. Defined as the height where the alongstream velocity  $u$  is reduced to half of the maximum velocity of that mooring velocity profile, the “kinematic interface height” (Hansen and Østerhus, 2007),  $H_{\text{IL}}$ , was 220 m at section C compared to ~~160~~ 110 m at S (see Figs. 5 and 6). The thinning of the plume with distance from the sill was reflected in both velocity and temperature profiles (Fig. 3). The height above bed of the  $3^\circ\text{C}$  isotherm was similar to  $H_{\text{IL}}$  (~~see Fig. 3~~), ~~correlated and correlated to it~~ over time scales longer than one day, as previously observed by Hansen and Østerhus (2007).

The high-velocity core of the plume was also faster but thinner at the southern ~~moorings of each side of the C~~ array. Long-term mean velocities were thus higher at mooring C3 than C2, ~~and higher at S3 than S2~~, while the opposite was true for the thickness of the high-velocity layer. This is consistent with observations by Hansen and Østerhus (2007) showing a northward decrease in velocity and increase in plume thickness across a section at the sill in the FBC ( $\sim 25$  km upstream of our measurements). (At the S array the velocities were similarly higher at S3 than at S2, but no southward thinning of the plume was observed, see Fig. 4.)

Although high instantaneous current velocities occurred at intermediate and upper levels, the flow above the plume was characterized by oscillations and frequent reversals,

resulting in weak mean flows (Figs. 1 and 3). The [varying upper layer currents contribute to modulating the period of mesoscale oscillations \(Darelius et al., 2015\)](#). The upper level mean current was generally directed along the plume, i.e. north-westerly, except for very weak flows in the opposite direction at the southernmost moorings in the S array. The mean counter-flow above 150 mab at mooring S4 was less than  $2.5 \text{ cm s}^{-1}$ .

In the centre of the C array (mooring C2) ~~currents~~ [daily current vectors](#) were always directed along-plume in the bottom 200 m. Above that, occasional reversals occurred, although rarely within 300 m above the seabed (Fig. 5). C1 was located near the northern edge of the plume in the channel, characterized by weaker currents and frequent reversals.

## 4 Volume transport

The volume transport of water in different temperature classes was estimated for mooring sections C and S from the gridded fields as described in Appendix B. [Time series of daily transport across sections C and S are shown in Fig. 7](#). Considering only the period ~~for which all mooring records were complete at both arrays, 29~~ [with complete vertical coverage of velocity of the cold overflow plume at all C-array moorings \(see Appendix B\), 30](#) May 2012–17 January 2013, the mean transport of overflow water at section C was  $1.3 \pm 0.3 \text{ Sv}$ , where  $\pm$  is the standard deviation of ~~daily values~~ [the daily resolution time series](#). The standard error of the overflow transport was  $0.1 \text{ Sv}$ , assuming independent records approximately every 4 days (the typical integral time scale and the time scale of mesoscale variability).

The overflow plume is subject to mixing and entrainment along its path leading to changes in the water mass properties of the core (e.g. Saunders, 1990; Mauritzen et al., 2005; Fer et al., 2010). As a result, the transport of the coldest plume water ( $< 0^\circ \text{C}$ ) was reduced from a mean of  $0.3 \pm 0.2 \text{ Sv}$  at section C to nil at S. The mean transport of modified overflow water at mooring section S was  ~~$1.8 \pm 0.7$~~   [\$1.7 \pm 0.7\$](#)  Sv. A wider temperature range (up to  $6^\circ \text{C}$ ; see Sect. 2) was considered here in order to account for the entrained water. From section C to section S, the  $T \leq 3^\circ \text{C}$  part of the transport decreased by  $0.5 \text{ Sv}$  and the  $3^\circ \text{C} < T \leq 6^\circ \text{C}$

class increased by 0.4 Sv, suggesting detrainment and entrainment, respectively, in the two layers, consistent with the budget results obtained in Sect. 6.2.

## 5 Temporal variability

### 5.1 Variability in different frequency bands

Current velocities and hydrographic properties varied strongly on different time scales. Velocity power spectra (not shown) displayed a distinct peak at the semi-diurnal tidal frequency at all moorings. In addition, the C array of moorings showed a diurnal tidal peak. There was also elevated power spectral energy in the frequency band corresponding to mesoscale oscillations. The mesoscale spectral peak was found at frequencies corresponding to 4–8 day at C, and 3–6 day at S.

Time series of monthly mean temperature at 8025 mab from moorings along the main plume path are shown in Fig. 8. Although this frequency band contains only a small part of the variability (about 5% for the series low-pass filtered with a 2 month cut-off compared to about 40% in the mesoscale frequency band) there is a consistent pattern between the different moorings.

The temperature in the bottom layer (Fig. 8) was lower than average during August through October 2012 at both section C and further downstream; ~~at moorings M1 and S2, October was the coldest month, with a monthly mean temperature of more than 0.5°C below the long-term mean.~~ Warmer than average temperatures persisted from November 2012 to February 2013 at mooring C2 and through April at M1 and S2. The maximum temperature in the bottom layer occurred in December at C2, and ~~in February~~ December through February was also a warm period at M1 and S2. After the warm winter months, the temperature decreased in early spring to a minimum in May. At mooring S2 the monthly mean temperature during this coldest month was about 0.5 °C below the long-term mean.

The variation in monthly bottom layer temperatures might be interpreted as a seasonal cycle, with generally higher temperatures in the winter months and low temperatures the

rest of the year. The temperature in July, however, deviated from this pattern by being clearly above the long-term mean at both section C and S (with maximum monthly temperatures recorded at M1 and S2), in sharp contrast to the low mean temperature of August.

Volume transport varied strongly on daily to monthly time scales (Fig. 7), but did not show a distinctive seasonal cycle (Fig. 9). The daily mean transport of water colder than  $3^{\circ}\text{C}$  ranged between 0.7 and 2.3 Sv at section C. The frequency spectra of volume transport through the arrays are shown in Fig. 10. Transport of cold water through section S varied most strongly at the time scale of mesoscale oscillations, while at section C low-frequency variation (~~and diurnal and semidiurnal tidal frequencies, not shown~~) dominated the transport spectrum. The month-to-month variability in volume transport ~~of cold water ( $< 3^{\circ}\text{C}$ )~~ was largely in phase between sections C and S, with maxima ~~in plume transport, as well as in total transport~~, at both sections in August and minima in November 2012 (Fig. 9).

## 5.2 Mesoscale variability

Figure 11 shows a subset of the data from the mooring array S, showing lateral temperature changes with time along the section. This mesoscale variability is typical of the entire record. The plume takes the form of domes of cold water moving past the mooring array, as previously noted by Geyer et al. (2006) and Darelius et al. (2011). While the presence of cold water at mooring S2–S4 was associated with downslope velocities, it was associated with upslope movement at mooring S1. Velocity vectors rotated mainly clockwise at S1 and S2, and anti-clockwise at S3 and S4.

There were energetic fluctuations in volume transport in the mesoscale frequency band, particularly strong at section S (Fig. 10). At section C, it was mainly the transport of overflow water ( $T < 3^{\circ}\text{C}$ ) that showed higher energy at mesoscale frequencies; at section S, there was high mesoscale variability also in the layer containing modified overflow water. The frequencies in the mesoscale band that are associated with elevated spectral energy levels correspond to periods of about three-four days and about six days, respectively. Darelius et al. (2015) have recently shown that the oscillations in the channel alternate over time

between these two periods, and that time periods dominated by the higher oscillation frequency (3–4 days) coincide with larger volume transport [across the sill](#).

The mean eddy heat flux in the mesoscale band was calculated following Voet and Quadfasel (2010). The mooring records were rotated to align with the mean current 100 mab and band-pass filtered (2–10 days) to obtain fluctuations  $v'$  and  $T'$  in the dominant mesoscale frequency band. Finally the mean temperature flux  $\overline{v'T'}$  were calculated at levels where both velocity and temperature data were available (Fig. 12a). The temperature fluxes were multiplied with the density ( $\rho_0$ ) and heat capacity ( $c_p$ ) to obtain heat fluxes and then integrated up to the deployment mean position of the 6 °C isotherm (numbers adjacent to moorings in Fig. 12b). The position of the isotherm was above the mooring at C3 and roughly at the level of the instrument at S1 (80 mab); no value was therefore calculated for C3 while the value in parenthesis at S1 is estimated assuming a constant value of the eddy heat flux from the bottom up to 80 mab. The temperature fluxes were mostly directed upslope, i.e. to the right of the mean current, and their magnitude was on the order of  $0.1 \text{ K m s}^{-1}$  reaching a maximum of  $0.21 \text{ K m s}^{-1}$  at S3, 70 mab.

Downstream of the Denmark Strait overflow, eddy heat fluxes were shown to be convergent in the central part of the plume (Voet and Quadfasel, 2010) indicating that the horizontal stirring induced by the eddies there contributed significantly to the observed along-path warming of the plume. This was not in general true for the FBC region: Fig. 12b shows divergence between S4 and ~~S2~~[S3](#), i.e. in the central and lower part of the plume, while the observations suggest convergence between C2 and C1 and between ~~S2~~[S3](#) and S1, i.e. for the shallow part of the plume.

## 6 Diapycnal mixing

### 6.1 Stability

The FBC overflow is a strongly sheared bottom-enhanced current characterized by energetic turbulence (Fer et al., 2010; Beaird et al., 2012). Our unique data set is used here

to present the kinematic stability in different layers of the water column throughout one year. The gradient Richardson number,  $Ri$ , representing the stability of stratified shear flow (Thorpe, 2007), is calculated over 10 m vertical scale using the hourly and 1 m vertical gridded velocity and temperature profiles. Density is inferred from the temperature as described in Sect. 2. Calculations are made using data from two moorings, each sampling the core of the dense overflow plume: C2 at the channel, and S2 over the slope. For each hourly profile, the depth of the 1 to 6 °C isotherms is identified. Vertical 10 m segments centered at the corresponding depths are extracted. Vertical gradients of density and of horizontal components of the velocity are obtained as the slope of the linear fit against depth. Hourly  $Ri$  is then calculated as  $N^2/S^2$  from the vertical velocity shear squared,  $S^2 = \left(\frac{\partial u}{\partial z}\right)^2 + \left(\frac{\partial v}{\partial z}\right)^2$ , and the buoyancy frequency  $N = \left[\left(\frac{-g}{\rho_0}\right) \left(\frac{\partial \sigma_\theta}{\partial z}\right)\right]^{1/2}$ . Monthly averages and standard deviations are then obtained after excluding outliers (the lowest and top 1 % quantiles) in each month. Standard error is assigned using the standard deviation and degrees of freedom assuming that every 13th sample is independent (to account for the semidiurnal variability).

The FBC overflow is characterized by small values of  $Ri$ . Very frequently, 60–80 % of the time, hourly  $Ri$  on the slope was below 1 and 10–30 % of the time  $Ri$  was below 1/4. In the channel, the core of the plume was associated with a 150 m thick high velocity layer with weak shear, typically with temperatures less than 3 °C. Despite the weak shear, stratification was low and monthly-averaged  $Ri$  varied between 2 and 4 (Fig. 13d). In the sheared interfacial layer monthly  $Ri$  was approximately 2 or less, and in the sheared bottom boundary layer monthly  $Ri$  was approximately 1 or less (the bottom boundary layer is not captured by the 1 °C class, hence is not shown in Fig. 13d).

Microstructure measurements reported in Fer et al. (2010) show that (i) the interior core of the plume in the channel is characterized by low dissipation rates, due to weak shear and lack of turbulent kinetic energy production, and (ii) turbulence is enhanced in a 100 m thick high-shear bottom layer and 100 m thick interfacial layer.  $Ri$  values derived from C2 are consistent with these measurements and imply that, in our analysis, values of  $Ri$  approximately 2 and less can be associated with energetic, turbulent regions of the water column.

In the channel, the 3 °C isotherm capped the low-shear core of the plume and  $Ri$  was typically above 2 throughout the year. The interface above, however, was turbulent at all times, and particularly in May with average  $Ri < 1$ . In contrast to the channel profiles, the low-shear core did not exist over the slope (Fig. 14).  $Ri$  was typically less than 2 below the 4 °C isotherm which separated the relatively quiescent stratified layer above (the 6 °C isotherm was characterized by average  $Ri > 2$  throughout the year). The vertical distribution of turbulence in the overflow thus differs between the channel section and the slope section.

## 6.2 Heat budget estimation of entrainment/detrainment

From each mooring array (C and S), daily averages of volume transport, mean temperature, layer thickness, and cross-section area binned in temperature classes were used to construct a [-volume-averaged](#) heat budget for the time period spanned by both arrays (29 30 May 2012–17 January 2013). [The budget method assumes a steady state and follows Hogg et al. \(1982\) and Whitehead and Worthington \(1982\)](#). Two layers were considered: one delineated by the seabed and the 3 °C isotherm and the other one above it, bounded by the 3 and 6 °C isotherms. Mooring array C defines the inflow section while array S is the outflow section of the control volume (see Fig. 15).

[The In steady state, the](#) volume budget can be written as

$$Q_{Bi} = Q_3 + Q_{Bo} + Q_{EK} \quad (1)$$

$$Q_{Ui} + Q_3 = Q_6 + Q_{Uo}, \quad (2)$$

where indices B and U refer to the bottom and upper layers, respectively; i refers to inflow (through array C) and o refers to outflow (array S), [and all quantities are time averaged over a suitable time window. The inflow and outflows are first integrated vertically over the layer, and then horizontally across the section before time averaging. Spatial and temporal averaging operators are omitted from the equations for simplicity.](#)  $Q_{EK}$  is the bottom Ekman transport, and  $Q_3$  and  $Q_6$  are the [average](#) vertical transports (positive upward) across the 3 and 6 °C isotherms, respectively.

The heat budget can then be expressed, using the time averaged quantities, as

$$Q_{Bi}T_{Bi} = F_{H3} + 3Q_3 + Q_{Bo}T_{Bo} \quad (3)$$

$$Q_{Ui}T_{Ui} + F_{H3} + 3Q_3 = F_{H6} + 6Q_6 + Q_{Uo}T_{Uo}. \quad (4)$$

~~Turbulent vertical heat flux across an isotherm is~~ In this section we use kinematic heat flux, that is the temperature flux  $vT$ . The diffusive heat flux, averaged over volume and time, is approximated as  $F_H = -K_z (dT/dz) L W$ , where  $K_z$  is the vertical eddy average vertical diffusivity,  $L$  is the horizontal along-path separation between the arrays,  $W$  is the average plume width defined by the given isotherm, and  $dT/dz$  is the average vertical temperature gradient. This approximation is typically invoked in the budget calculations, and is valid if the local values of diffusivity and the vertical temperature gradient are not correlated. Our resulting estimates of average vertical diffusivity should thus be interpreted with this caveat in mind.  $L$  was chosen as 60 km. In the calculations we used transport weighted temperature for the layers (see e.g. Duncan et al., 2003).

~~The budget was calculated using daily averaged data in 30 day windows to sufficiently average over the 3–5 day mesoscale variability. This formulation of the heat budget thus does not include eddy fluxes discussed in Sect. 5.2.~~ For each layer,  $dT/dz$  is calculated as the difference between (transport weighted) average temperature divided by the difference in average thickness in each layer. We assumed that the upper layer underlies a 50 m thick top layer at a temperature of 7.5 °C.

The budget was calculated using averages over 30-day long segments of the daily time series which are moved by 1 day throughout the record (that is, 1-day moving 30-day width windows). The 30-day window sufficiently averages over the 3-5 day mesoscale variability. While the steady-state assumption is questionable, the variability in section volume transports is mainly contained in time scales less than 10 days (see Fig. 10 for the variance-preserving transport spectra). Budget calculations using time average windows from 5 days to 3 months with 5-day increments (not shown) confirm that the results are not sensitive to the choice of the 30-day window after approximately 15-25 days. We thus expect the budget calculations to be fairly representative of the steady state, and to yield a more

accurate estimate of entrainment rates compared to analysis of snapshots of hydrography and currents from single cruises. Because the mesoscale variability is averaged, the eddy fluxes discussed in Sect. 5.2 are not included in the formulation of the heat budget. The Ekman transport  $Q_{EK} = (C_D V^2 / f) L$ , where the drag coefficient  $C_D = 3.7 \times 10^{-3}$  is from direct turbulence measurements of the FBC overflow (Fer et al., 2010), and  $V$  is the spatial mean flow of the plume at the given time. For  $V$  we use an average over both the bottom and upper layers and over both arrays (average transport divided by average cross section area). The results are not sensitive to using only the bottom layer average. The long-term mean value of  $Q_{EK}$  estimated in this way was 0.3 Sv.  $Q_{EK}$  does not enter-contribute to the heat budget because the near-bottom temperature is approximately  $0^\circ\text{C}$ , and thus equal to the reference temperature.

The magnitude of the different terms in the budget can be compared to justify the exclusion of lateral eddy fluxes and the heat flux associated with  $Q_{EK}$ . The average advective heat fluxes,  $QT$ , and diffusive heat fluxes  $F_H$  are on the order  $1 \text{ Sv } ^\circ\text{C}$  with one order of magnitude smaller standard deviation.  $QT$  in the upper layer is 2 (Section C) to 4 times (Section S) larger than the values in the bottom layer (approximately  $1.3 \text{ Sv } ^\circ\text{C}$  at both sections), and the diffusive fluxes are approximately  $0.7 \text{ Sv } ^\circ\text{C}$  downward, across each layer. In comparison, the bottom Ekman heat flux averaged over both sections is  $-0.02 \text{ Sv } ^\circ\text{C}$ , hence negligible. Using the magnitudes given in Fig. 12, the net average eddy heat flux integrated to the  $6^\circ\text{C}$  isotherm, averaged over both sections is on the order  $100 \times 10^5 \text{ W m}^{-1}$ , or integrated over  $L = 60 \text{ km}$  (and converting to temperature flux) is  $0.15 \text{ Sv } ^\circ\text{C}$ . The uncertainty is not quantified and is possibly large. Nevertheless, the eddy heat flux term is one order of magnitude less than the advective heat fluxes and approximately 20% of the diffusive flux. The contribution of the eddy heat flux to the heat budget is probably much less since the rotational component of the eddy flux is not removed (see Sect. sec:discussion).

The heat budget was used to estimate rates of entrainment and detrainment (Fig. 16a). Throughout the whole period there was always detrainment from the bottom layer and entrainment into the upper layer:  $Q_3$  was positive throughout with a long-term mean of 0.2 Sv and  $Q_6$  negative with a mean of  $-0.2 \text{ Sv}$ . Entrainment in the upper layer peaked in June and

August, and was at minimum levels in October and December. December was also a time of minimum detrainment in the bottom layer.

The mean ~~eddy~~-vertical diffusivities inferred from the heat budget were  $(119 \pm 43) \times 10^{-4}$   $(120 \pm 43) \times 10^{-4} \text{ m}^2 \text{ s}^{-1}$  for the bottom layer and  $(30 \pm 15) \times 10^{-4} \text{ m}^2 \text{ s}^{-1}$  for the upper layer. The sensitivity of these results to the choices of various parameters in the heat budget was tested. Increasing the value of  $L$  chosen to represent the distance between the mooring arrays by 10% reduced  $K_z$  in each layer by 8–9%. An increase in assumed thickness of the top layer overlying layer U from 50 to 100 m led to an increase in mean  $K_{zU}$  by 14%, while keeping the thickness at 50 m and instead increasing the temperature by 1 °C reduced the mean  $K_{zU}$  by 20%. Determining  $dT/dz$  from temperature and thickness values at only one mooring array, instead of averaging over both, led to a 13% increase (using values from C) or decrease (values from S) in  $K_{zU}$ . The sensitivities are thus less than the error bounds (one standard deviation) given for  $K_z$ .

## 7 Discussion

The topography, with the narrow channel opening onto the Iceland–Faroe slope, affects the anatomy and mixing of the FBC overflow. The overflow plume became markedly thinner between mooring section C and S. Not only the average temperature, but also the shape of both the velocity and temperature profiles changed so that the thickness of the well-mixed bottom layer decreased (see Fig. 3). The reduction in height reflects the spreading and thinning of the plume on the open slope after escaping the topographic constraint of the channel. The thinning of the plume with distance downstream was accompanied by increased velocities (see Figs. 5 and 6), as previously observed by e.g. Mauritzen et al. (2005) and Duncan et al. (2003).

Inside the thick core of the plume in the channel, there was a 150 m-thick weak shear layer. As shown by Fer et al. (2010), the flow in this layer was relatively stable (higher  $Ri$ ) compared to the more turbulent layers above and below it (in the interface and towards the bottom, respectively). The thinner and faster plume at section S, however, had no such qui-

escent layer. The low values of  $Ri$  (average  $< 1$  throughout the year) below about 150 mab at S and for a layer centred at about 300 mab at C demonstrate the high potential for turbulence generation due to the strongly sheared flow, despite the strong stratification. Similar results from earlier process studies (Borenäs and Lundberg, 1988; Saunders, 1990; Fogelqvist et al., 2003; Fer et al., 2010) are thus corroborated by our longer-term data set.

At ~~both mooring sections~~ the mooring section in the Channel, the plume was faster, thinner, and colder toward the southern (Faroe Bank) side of the section. This is in agreement with the observation by Hansen and Østerhus (2007) that the core velocity decreases and the thickness of the plume increases toward the right (looking downstream), and is a typical structure for a gravity current confined to channel in a rotating system (cf. Guo et al., 2014). The stronger thermal stratification found on the southern side ~~of the mooring arrays~~ is an example of the “isotherm pinching” observed on the southern side of the Channel (e.g. Borenäs et al., 2001).

In classical descriptions of dense overflows, the volume transport of an overflow is assumed to increase gradually – or abruptly at mixing hot spots – due to entrainment of the overlying waters (Price and O’Neil Baringer, 1994; Legg, 2012). For the FBC overflow, intensive mixing has been observed in locations just west of the channel exit (Duncan et al., 2003; Mauritzen et al., 2005; Fer et al., 2010; Beird et al., 2012). The mixing results in large changes in water mass properties; south of Iceland the boundary current contains only about half overflow water, and half admixed upper layer water (Fogelqvist et al., 2003). If there was no detrainment (as suggested by Mauritzen et al., 2005), a doubling of the overflow volume transport might thus be expected (Hansen and Østerhus, 2007). On the basin scale, the total transport of Iceland Scotland Overflow Water increases with distance along its path through the North Atlantic by on average 1.8 Sv over 1000 km (Kanzow and Zenk, 2014, this would correspond to 0.1 Sv between sections C and S). Mauritzen et al. (2005) observed an increase in dense water transport (although the densest classes vanished) between CTD sections progressing downstream in the FBC outflow region. A recent model study of the FBC overflow by Guo et al. (2014) showed a downstream increase in overflow volume transport (for temperatures  $\leq 6^\circ\text{C}$ ) of about 0.6 Sv over 90 km.

Our unique data set shows our data set, however, that the simplified view of along-path volume increase is not accurate for the FBC overflow. As the plume proceeds into the stratified ambient water, there is substantial detrainment from the deeper layer, of comparable magnitude to the entrainment into the interfacial layer. Our estimated shows no corresponding increase from mooring array C to array S. To explore this surprising result, we must first ask ourselves whether our measurements covered the entire plume at both sections.

At array C, overflow water on average occupied the lower 120 m at the southernmost mooring (see section 3). The southern boundary of the plume must thus be south of the mooring section, but because the flow here is constrained by topography the plume cannot extend far to the south. Our horizontal extrapolation adequately compensates for the edges of the plume; our mean volume transport of estimate for water colder than  $3^{\circ}\text{C}$  north-westward through the FBC was of  $1.3 \pm 0.3 \text{ Sv}$  at mooring array C. This value for the mean transport at C is within the range of earlier estimates for the FBC overflow varying between 1.1 and is within the range of earlier estimates for the FBC overflow varying between 1.1 and  $2.1 \text{ Sv}$  (van Aken and Becker, 1996; Hansen and Østerhus, 2000; Kanzow and Zenk, 2014) (van Aken et al., 2015). The estimated volume transport at array C is about 2/3 of the kinematic overflow estimate at the sill (Darelius et al., 2015, and Appendix B).

The S section was not located in the channel, but on the open slope. The question of how that mooring array was positioned with respect to the plume path is therefore important. First, we consider the statistics of the observed temperature and velocity at the moorings at section S. There was a clear presence of overflow water throughout the year at the two moorings S2 and S3 in the centre of the array, while at the two moorings at the edges, cold plume waters were only occasionally present. At the northernmost mooring, S1, overflow waters ( $T < 3^{\circ}\text{C}$ ) were found at 80 mab (the only measurement level here) less than 10% of the time and modified overflow waters ( $T < 6^{\circ}\text{C}$ ) less than 35% of the time. At the southernmost mooring, S4, the corresponding percentages at the same height above seabed were less than 2% for  $T < 3^{\circ}\text{C}$  and about 36% for  $< 6^{\circ}\text{C}$ . At both moorings, the

lowest temperatures were correlated with stronger along-stream velocity, a clear indication of plume presence at such occasions. Cold water was present at these moorings only during periods with energetic oscillations (Darelius et al., 2015), suggesting that it is brought here by the eddy motion. Most of the time, however, the overflow was found in the centre of the array while absent at the outer moorings (i.e. the boundaries of the plume were found within the mooring array).

While there are no channel walls here to contain the overflow, the shallow topography north of array S likely prevents large excursions of the plume to the north (upslope). There is no evidence in literature of a plume path north of mooring S1. The mean current of the overflow mainly follows isobaths (Geyer et al., 2006), until it begins to descend under the influence of friction (Seim et al., 2010). Are there then downslope excursions that make the overflow pass south of section S? As mentioned above, the occurrence of cold water at mooring S4 was rare, and the long-term average velocity there was approximately zero (see figures 1 and 3). Our observations thus do not show any evidence of significant overflow at (or beyond) the southern end of array S.

A second important issue to consider is the bifurcation of the flow. The overflow is known to split into two branches. The shallower branch flows westward, approximately following the isobaths along the Atlantic flank of the Iceland–Faroe Ridge, and the deeper branch turns southwestward, and descends more directly into the southern Iceland Basin (Beird et al., 2013; Hansen and Østerhus, 2000). The splitting appears to occur between the secondary sill at about 9°W and a topographic “bump” or plateau further downstream (Mauritzen et al., 2005; Beird et al., 2012, 2013). In designing our mooring array S, we chose a location to the east (i.e., upstream relative to the overflow) of the suspected bifurcation location to ensure an as complete as possible lateral coverage of the plume. Could the weak flow at mooring S4 indicate that the bifurcation occurred upstream of array S and that S4 thus was located between the branches? We turn to literature to find out where this bifurcation is most likely to occur.

Repeat hydrographic sections from the multi-vessel “Overflow” survey in June 1960 (Lee, 1967; Tait, 1967) showed the cold

core of the overflow centred at about 800 m depth, 10°W (station F1 at 61° 54'N, 10° 06'W – very close to the 'bump' centred at 61° 54'N, 10° 07'W; cf. Beirid et al., 2013). However, maps of overflow thickness and percentage overflow water based on the same survey data suggested a bifurcation of the overflow beginning already upstream of this (see figures 3:108 and 3:109 in Hermann, 1967). Synthesizing the observations of the 1960 survey, the "Overflow 1973" experiment (Müller et al., 1979), and some evidence from geological studies, Hansen and Østerhus (2000) suggested an "alternative path" (see their fig. 43 and 49) for the overflow, turning southwestward and descending more directly and deeper in the (south-eastern) Iceland Basin. In a more recent study, the bottom temperature distribution measured by gliders indicated a branch of the overflow descending deeper than 1000 m, somewhere in the region close to our mooring section S (purple line in fig. 17; cf. Beirid et al., 2013). This branch appeared to the west of our array S, and could not be resolved because of 1000-m depth rating of the gliders.

During a survey conducted in June 2000, Mauritzen et al. (2005) found dense waters and high velocities as deep as between the 1000 and 1200 m isobaths at their section G, only about 5 km downstream of our array S (fig. 17, for comparison, mooring S4 was located at a depth of 1082 m). The authors remark, however, that the occupation of section G shown in the paper (their figures 23 and 24) took place after a storm when the overflow transport doubled. A better temporal averaging is provided from the survey in June 2012 reported in Ullgren et al. (2014). In a section repeated five times over the course of 70 h, located about 10 km upstream of our mooring array S, the high-velocity core of the overflow was mostly centered close to, or shallower than, the 1000-m isobath, with reduced flow at the outer two stations (Ullgren et al., 2014).

Mauritzen et al. (2005) mention that a division into two branches at about 900 m depth is indicated at their westernmost section, H, located about 50 km downstream of our array S. (Section H is marked by green dots but not labelled in figure 17; it is the section the lower part of which is parallel and close to Geyer's section A.) They suggest that the bifurcation occurs somewhere between their sections G and H, where the flow decelerates and is "separated by a plateau in the topography" (Mauritzen et al., 2005, p. 910). Most likely this

flow separation is thus caused by the same topographic feature as Beird et al. (2013) refer to as the 'bump' (see fig. 17).

Mean current velocity vectors from July–November 1999 presented by Geyer et al. (2006) show a split into two branches at about  $11^{\circ}\text{W}$  (their Fig. 3), also west of our mooring section S (see Fig. 17). Note that this is a split of a deeper flow around a different topographic feature, southwest of the bump of Beird et al. (2013). The location of the knoll dividing the flow in the paper by Geyer et al. (2006) fits with the observation by Swift (1984) that data sets from the Overflow 1960 and 1973 expeditions (Tait, 1967; Müller et al., 1979) both show a "similar three-way splitting of the overflow tongue at about  $61^{\circ}45'\text{N}$  and  $11^{\circ}\text{W}$ ".

The complex topography that varies strongly on small scales is a major factor controlling overflow pathways in simulations (Chang et al., 2009). Tracer-weighted average plume paths from model experiments by Seim et al. (2010) and Riemenschneider and Legg (2007) generally turn more southward and descend below the 1000 m isobath close to (but typically west of) the location of array S.

Further evidence of the overflow splitting into a deeper and a shallower branch in the region just west of array S is found in velocities measured at 64 mab by a deep towed vehicle (Fig. 7 in Duncan et al., 2003). The current below about 900 m veered downslope at a section located about 20 km downstream of array S (Fig. 17). Two out of the three bottom-following float trajectories shown by Prater and Rossby (2005) followed roughly along the 1000-m isobath until at least  $11^{\circ}\text{W}$ , while one track descended earlier (closer to mooring array S). It should be noted that for the latter, as well as for one of the other floats, the positions along this part of the track were only estimates, not directly determined by sound ranging.

We conclude that while the mooring array S is located in the region where the FBC overflow divides into two branches, a detailed comparison with earlier work suggests that the split takes place downstream of array S. We are reasonably confident that mooring array S did not miss a branch of the overflow because the bifurcation (or one bifurcation) is most likely caused by the topographic bump centred at about  $61^{\circ}54'\text{N}$ ,  $10^{\circ}7'\text{W}$ , approximately

30 km downstream of array S. The deeper branch of the overflow and its path into the Iceland Basin merit further studies.

Our unique data set shows, then, that the simplified view of along-path volume increase is not accurate for the FBC overflow. As the plume proceeds into the stratified ambient water, there is substantial detrainment from the deeper layer, of comparable magnitude to the entrainment into the interfacial layer. Although the maximum plume velocity was measured at the downstream array, the volume transport of plume water with  $T \leq 3^\circ\text{C}$  decreased to  $0.8 \pm 0.4 \text{ Sv}$  at section S. As expected, the volume transport of the coldest waters disappeared ( $T \leq 0^\circ\text{C}$ ) or was reduced ( $0^\circ\text{C} < T \leq 10^\circ\text{C} < T < 1^\circ\text{C}$ ) between section C and section S. ~~Reduction~~ A reduction in the low temperature classes of FBC overflow transport within the first few hundred kilometres downstream of the sill was shown by Duncan et al. (2003), while Beaird et al. (2013) found a downstream decrease in transport regardless of water class definitions used. Similarly, Fer et al. (2010) found no increase ~~in boundary layer transport~~ volume transport in the bottom cold layer despite dilution typically indicating entrainment. They suggested that the dilution might instead be caused by warmer interface layer water being supplied to the bottom layer by the transverse circulation, replacing bottom water lost through bottom Ekman drainage. Throughout our year-long measurements, there was persistent detrainment from the bottom layer and entrainment into the interfacial layer; the decrease in cold water transport between sections C and S was compensated by a roughly equal increase of transport in the intermediate temperature range  $3^\circ\text{C} < T \leq 6^\circ\text{C}$ . The total mean transport ~~at temperatures below  $6^\circ\text{C}$  of overflow and modified overflow together~~ thus did not change between the channel and the slope sections. This finding may have important implications considering the role of the FBC overflow in the production of North Atlantic Deep Water and for assessing changes in the global thermohaline circulation (Hansen et al., 2001; Dickson et al., 2002). Simple estimates of the contribution of the FBC overflow to the global thermohaline circulation assume doubling of the volume transport due to entrainment. Our observations suggest that despite substantial entrainment, volume transport does not increase significantly because of detrainment,

implying that the impact of FBC overflow on the global thermohaline circulation can be less than what has usually been assumed.

No clear seasonal cycle was detected in the volume transport of the FBC overflow, but there was variability at monthly time scales. Transport peaked at both sections in June and August 2012, coinciding with maximum entrainment into the upper layer. Minimum entrainment in the upper layer occurred in October 2012, a month that was marked by minimum bottom layer temperatures both at section S and the mid-mooring M1. Saunders (1990) found no seasonality of plume thickness, temperature or velocity in year-long measurements, but Hansen and Østerhus (2007) showed a seasonal variation of kinematic overflow at the sill of about 10% of the mean over a 10-year period. The relatively low amplitude of the seasonal cycle compared to shorter-term variations means it only becomes apparent in data sets covering several years. The seasonal variability in the outflow has been linked to seasonality in the barotropic northward flow of Atlantic Water in the Faroe–Shetland Channel (Lake and Lundberg, 2006) . Darelius et al. (2015) showed that variability in volume flux on shorter time scales is linked to the local barotropic forcing.

Mean diffusivities inferred from the two-layer heat budget constructed for the overflow ,—were  $(30 \pm 15) \times 10^{-4} \text{ m}^2 \text{ s}^{-1}$  for the upper layer and  $(119 \pm 43) \times 10^{-4} (120 \pm 43) \times 10^{-4} \text{ m}^2 \text{ s}^{-1}$  for the bottom layer, were in within the range of values observed during research cruises in 2010 and 2012 (Fer et al., 2010, 2014). Earlier estimates have ranged between 50 and  $500 \times 10^{-4} \text{ m}^2 \text{ s}^{-1}$  (cf. Saunders, 1990; Duncan et al., 2003); however, they suffer from not resolving the mesoscale variability. The eddy-vertical diffusivity in both layers show a factor of 5 increase in late August and late December. These changes coincide with periods of high eddy kinetic energy reported in Darelius et al. (2015), suggesting that the energetic mixing is associated with mesoscale variability.

Guo et al. (2014) propose that the mesoscale variability in the FBC is caused by baroclinic instability of the plume. In their model experiment, the baroclinic instability and resulting variability are energized downstream of the sill, and high baroclinic conversion rates occur

40–60 km downstream of the sill. This is consistent with our Fig. 10, which shows more energetic mesoscale transport fluctuations at section S than at C.

Eddy heat fluxes were divergent in the central and deep part of the plume and convergent between the northernmost (upper) moorings on each section, indicating that the effect of eddy heat transports is a net cooling of the deep part of the plume and a net warming of the shallower part. The observed temperature fluxes on the order of  $0.1 \text{ K m s}^{-1}$  were about ten times larger than the values reported by Voet and Quadfasel (2010) from the region downstream of the Denmark Strait overflow and in agreement with values reported by Darelius et al. (2011) and the modelled values by Guo et al. (2014). Since density is largely determined by temperature in the FBC, the upslope temperature flux is equivalent to an upslope buoyancy flux i.e. a release of potential energy. This is consistent with eddy generation due to baroclinic instability, shown by Guo et al. (2014) to be the mechanism at play in the FBC. The observed heat or buoyancy fluxes are the sum of a (dynamically unimportant) rotational component and residual, divergent component which is the one responsible for the energy conversion (Marshall and Shutts, 1981). While our data set does not allow us to separate the two components, we note that, in this region, the total flux field and the divergent flux field are relatively similar in the model study by Guo et al. (2014).

## 8 Conclusions

One-year long moored measurements of currents and hydrographic properties in the overflow region of the Faroe Bank Channel (FBC) have provided time series of plume characteristics, volume transport and vertical mixing from two cross-sections along the path of the dense overflow plume. One section was located in the narrow channel (C) ~~constraining the overflow geographically, and the~~ that geographically constrains the overflow. The other section was on the slope (S) after the channel topography opens up but before the bumps or knolls at  $10^{\circ}07'W$  and  $11^{\circ}W$  where the plume is the most likely to split into several branches. The anatomy of the plume, the variability of velocity and hydrographic properties in space and time, as well as the mixing characteristics are found to differ between the

two sections. The volume transport through the slope section was dominated by mesoscale variability, while transport through the channel section was less strongly influenced by the 3–5 day oscillation. Inferred lateral heat (equivalent to buoyancy) fluxes, and the energization of the mesoscale variability with downstream distance from the sill are consistent with earlier findings supporting baroclinic instability of the overflow plume. The long-term mean overflow transport towards the Iceland Basin of waters colder than 3 °C was  $1.3 \pm 0.3$  Sv at section C. The transport at section S, consisting of modified overflow water with temperatures up to 6 °C, was  $1.8 \pm 0.7$  Sv. In the channel, turbulence was likely to be generated near the bottom and at the interface capping the relatively quiescent thick plume core. At section S, in contrast, the whole plume layer – here thinner but faster – was marked by low  $Ri$  values throughout the year. ~~Present~~ Based on a two-layer heat budget constructed for the overflow, mean diffusivities across the top of the bottom mixed layer, and across the interfacial layer are  $(30 \pm 15) \times 10^{-4} \text{ m}^2 \text{ s}^{-1}$  and  $(120 \pm 43) \times 10^{-4} \text{ m}^2 \text{ s}^{-1}$ , respectively. The present study provides a more accurate observational-based estimate of the volume transport, entrainment and eddy diffusivities associated with the overflow plume because the data set resolves the temporal variability and covers the entire lateral and vertical extent of the plume. ~~A simplified view of along-path entrainment of a gravity current is not valid for the FBC overflow~~ The contribution of the FBC overflow (and the dense Greenland–Scotland Ridge overflows in general) to the North Atlantic Deep Water is sometimes estimated based on an assumed doubling of the volume transport due to entrainment. Our data, although limited to a region close to the overflow site, suggest that this description is not accurate. As the plume proceeds into the stratified ambient water, there is substantial detrainment from the deeper layer, of comparable magnitude to the entrainment into the interfacial layer. ~~Based on a two-layer heat budget constructed for the overflow, mean diffusivities across the top of the bottom mixed layer, and across the interfacial layer are  $(30 \pm 15) \times 10^{-4}$  and  $(119 \pm 43) \times 10^{-4}$ , respectively~~ A simplified view of along-path entrainment of a gravity current is thus not valid for the FBC overflow. A more accurate quantification of the FBC overflow on the global thermohaline circulation merits further studies.

## Appendix A: Mooring data

### A1 Instruments and data return

Details of mooring positions and instrumentation are given in Table A1. The table also gives record lengths if shorter than the whole one-year deployment; for example in the case of the three ADCPs sampling at higher resolution (see Sect. 2).

### A2 Mooring movement and data interpolation

The strong currents caused mooring knockdown, statistics of which are presented in Table A2. Mooring knockdown events led to tilting of the instruments, occasionally more than the threshold values for acceptable tilt specified by the manufacturers:  $15^\circ$  for RDI-ADCPs and  $12^\circ$  for RCM. A gimbal on the RCM frame compensates for tilt of up to  $27^\circ$ , so the practical threshold limit is  $39^\circ$ . Data from periods with too large tilt are excluded from the analysis, causing a slight bias towards lower velocities (since the drag and thus the tilt is larger for larger velocities). The percentage of data discarded for each instrument is listed in Table A2.

## Appendix B: Transport calculation

The volume transport of water in different temperature classes was calculated for mooring sections C and S as follows. Temperature and rotated velocity records were low-pass filtered with a 3rd order Butterworth filter with a 27 h cut-off period, and daily averages were computed. Depth levels with less than 3070 % good data were excluded. At moorings shorter than 300 m, velocity and temperature profiles were extended to 300 mab using constant shear or a constant temperature gradient, respectively, above the top instrument (allowed to continue only to  $0 \text{ cm s}^{-1}$  or  $8^\circ\text{C}$ ). At S1, where there was only one instrument at 80 mab, velocity was set to decrease and temperature to increase linearly upwards to  $0 \text{ cm s}^{-1}$  and  $8^\circ\text{C}$ , respectively, at 300 mab. At C3, the downward-looking ADCP at 150

mab failed after 234 days of recording (Table A1), on 17 January 2013. Rather than trying to construct velocity records for most of the water column at this important location after that, we choose to compute volume transports only for the period in which we have vertical velocity profile coverage of the high-velocity bottom layer of the plume at all three C-array moorings. Velocities were linearly extrapolated downward to 0 at the bottom from the deepest instrument on each mooring. If this was located higher than 50 mab, velocity was kept constant from the deepest instrument down to 50 mab before decaying linearly from there to 0 at the bottom. Temperature was kept constant from the deepest instrument to the bottom. The resulting vertical profiles from all moorings on one array were then gridded on to a 5 m vertical by 1 km horizontal grid for each day using linear interpolation, with velocity set to 0 at the bottom grid point. To extend the section horizontally, data from the outer moorings in each array were kept constant to the sides over half the distance between moorings. The resulting gridded cross sections represent daily snapshots of the plume velocity and temperature structure. Volume transport in different temperature classes was estimated for each day by summing the transport contributions (the along-stream  $u$  velocity component multiplied by the corresponding cross-section area defined by the isotherms). Only  $u \leq 0$  was included; any reverse flow was not included in the plume transport calculation.

Sensitivity to different methods of inter- and extrapolating data to grids of varying resolutions were examined. Because the overflow is swift and the cross-sectional area is large, the results are not sensitive to the details of the choices for upper and bottom boundaries and plume edges. The transport obtained from the method described above ( $Q_{\text{grid}}$ ) was compared with those computed by two other methods (see Fig. A1). One method is to compute transport per unit width for each mooring, multiplying this by a representative width for each mooring, and then summing up the contribution of the individual moorings, as described in Darelius et al. (2011). This will be referred to as  $Q_{\text{moor}}$ . The other alternative method is to compute “kinematic overflow” ( $Q_{\text{kine}}$ ), defined in Hansen and Østerhus (2007) as the volume flux of water from the bottom up to the level at which the overflow velocity is reduced to half of the profile maximum. Changes in terms of vertical extrapolation and horizontal grid resolution had relatively small effects on the long-term mean values of transport

from the gridded fields. The transport time series  $Q_{\text{moor}}$  at C had the same long-term mean and standard deviation for the temperature range  $\leq 6^{\circ}\text{C}$  ( $1.8 \pm 0.4\text{ Sv}$ ) as  $Q_{\text{grid}}$ . The mean of  $Q_{\text{kine}}$  was somewhat higher,  $2.0 \pm 0.5\text{ Sv}$ . Similarly, Darelius et al. (2015) found that  $Q_{\text{moor}}$  at array C was somewhat lower than (but correlated to)  $Q_{\text{kine}}$  at the sill. Volume transports stated in the main body of this paper are  $Q_{\text{grid}}$ .

*Acknowledgements.* We thank the technicians involved in mooring preparation and deployment, H. Bryhni and S. Myking, and the crew of the R.V. *Håkon Mosby*. [Thanks also to two anonymous reviewers whose comments helped improve the manuscript.](#) This work was funded by the Research Council of Norway through the FRINAT programme, under project n.o 204867/V30 “Faroe Bank Channel Overflow: Dynamics and Mixing”.

## References

- Beird, N. L., Fer, I., Rhines, P., and Eriksen, C.: Dissipation of turbulent kinetic energy inferred from Seagliders: an application to the Eastern Nordic Seas overflows, *J. Phys. Oceanogr.*, 42, 2268–2282, doi:10.1175/jpo-d-12-094.1, 2012.
- Beird, N. L., Rhines, P. B., and Eriksen, C. C.: Overflow waters at the Iceland-Faroe Ridge observed in multiyear Seaglider surveys, *J. Phys. Oceanogr.*, 43, 2334–2351, doi:10.1175/JPO-D-13-029.1, 2013.
- Borenäs, K. and Lundberg, P.: The Faroe-Bank Channel deep-water overflow, *Deep-Sea Res. Pt. II*, 51, 335–350, 2004.
- Borenäs, K. M. and Lundberg, P. A.: On the deep-water flow through the Faroe Bank Channel, *J. Geophys. Res.*, 93, 1281–1292, 1988.
- Borenäs, K. M., Lake, I. M., and Lundberg, P. A.: On the intermediate water masses of the Faroe-Bank Channel overflow, *J. Phys. Oceanogr.*, 31, 1904–1914, 2001.
- [Chang, Y. S., Garraffo, Z. D., Peters, H. and Özgökmen, T. M.: Pathways of Nordic Overflows from climate model scale and eddy resolving simulations, \*Ocean Model.\*, 31, 66–84, 2009.](#)
- Darelius, E., Fer, I., and Quadfasel, D.: Faroe Bank Channel overflow: mesoscale variability, *J. Phys. Oceanogr.*, 41, 2137–2154, 2011.

- Darelius, E., Ullgren, J. E., and Fer, I.: Observations of barotropic oscillations and their influence on mixing in the Faroe Bank Channel overflow region, *J. Phys. Oceanogr.*, 43, 1525–1532, doi:10.1175/JPO-D-13-059.1, 2013.
- Darelius, E., Fer, I., Rasmussen, T., Guo, C., and Larsen, K. M. H.: On the modulation of the periodicity of the Faroe Bank Channel overflow instabilities, *Ocean Sci. Discuss.*, 12, 823–861, [11, 855–871](#), doi:10.5194/os-11-855-2015, 2015.
- Dewey, R. K.: Mooring Design and Dynamics – a Matlab package for designing and analyzing oceanographic moorings, *Marine Models*, 1, 103–157, 1999.
- Dickson, B., Yashayaev, I., Meincke, J., Turrell, W. R., Dye, S., and Holfort, J.: Rapid freshening of the deep North Atlantic Ocean over the past four decades, *Nature*, 416, 832–837, 2002.
- Dickson, R. R. and Brown, J.: The production of North Atlantic Deep Water: sources, rates and pathways, *J. Geophys. Res.*, 99, 12319–12341, 1994.
- Dooley, H. D. and Meincke, J.: Circulation and water masses in the Faroese Channels during Overflow '73, *Deutsche Hydrographische Zeitschrift*, 34, 41–55, 1981.
- Duncan, L. M., Bryden, H. L., and Cunningham, S. A.: Friction and mixing in the Faroe Bank Channel outflow, *Oceanol. Acta*, 26, 473–486, 2003.
- Fer, I., Voet, G., Seim, K. S., Rudels, B., and Latarius, K.: Intense mixing of the Faroe Bank Channel overflow, *Geophys. Res. Lett.*, 37, L02604, doi:10.1029/2009GL041924, 2010.
- Fer, I., Peterson, A. K., and Ullgren, J. E.: Microstructure measurements from an underwater glider in the turbulent Faroe Bank Channel overflow, *J. Atmos. Ocean. Tech.*, 31, 1128–1150, 2014.
- Fogelqvist, E., Blindheim, J., Tanhua, T., Østerhus, S., Buch, E., and Rey, F.: Greenland-Scotland overflow studied by hydro-chemical multivariate analysis, *Deep-Sea Res. Pt. I*, 50, 73–102, 2003.
- Geyer, F., Østerhus, S., Hansen, B., and Quadfasel, D.: Observations of highly regular oscillations in the overflow plume downstream of the Faroe Bank Channel, *J. Geophys. Res.*, 111, C12020, doi:10.1029/2006JC003693, 2006.
- Guo, C., Ilicak, M., Fer, I., Darelius, E., and Bentsen, M.: Baroclinic instability of the Faroe Bank Channel overflow, *J. Phys. Oceanogr.*, 44, 2698–2717, 2014.
- Hansen, B. and Østerhus, S.: North Atlantic-Nordic Seas exchanges, *Prog. Oceanogr.*, 45, 109–208, 2000.
- Hansen, B. and Østerhus, S.: Faroe Bank Channel overflow 1995-2005, *Prog. Oceanogr.*, 75, 817–856, 2007.
- Hansen, B., Turrell, W. R., and Østerhus, S.: Decreasing overflow from the Nordic seas into the Atlantic Ocean through the Faroe Bank channel since 1950, *Nature*, 411, 927–930, 2001.

- Hermann, F.: The TS diagram analysis of the water masses over the Iceland–Faroe Ridge and in the Faroe Bank Channel, *Rapp. PV Reun. Cons. Int. Explor. Mer.*, **157**, 139–149, 1967.
- Hogg, N., Biscaye, P., Gardner, W., and Schmitz Jr, W. J.: On the transport and modification of Antarctic Bottom Water in the Vema Channel, *J. Mar. Res.*, **40**, 231–263, 1982.
- Høyer, J. L. and Quadfasel, D.: Detection of deep overflows with satellite altimetry, *Geophys. Res. Lett.*, **28**, 1611–1614, 2001.
- Kanzow, T. and Zenk, W.: Structure and transport of the Iceland Scotland Overflow plume along the Reykjanes Ridge in the Iceland Basin, *Deep-Sea Res. Pt. I*, **86**, 82–93, 2014.
- Lake, J. and Lundberg, P.: Seasonal barotropic modulation of deep-water overflow through the Faroe Bank Channel, *J. Phys. Oceanogr.*, **36**, 2328–2339, 2006.
- Lee, A. J.: Temperature and salinity distributions as shown by sections normal to the Iceland–Faroe Ridge, *Rapp. PV Reun. Cons. Int. Explor. Mer.*, **157**, 100–135, 1967.
- Legg, S.: Overflows and convectively driven flows, in: *Buoyancy-Driven Flows*, edited by: Chassignet, E., Cenedese, C., and Verron, J., Cambridge University Press, Cambridge, UK, 203–239, 2012.
- Marshall, J. and Shutts, G.: A note on rotational and divergent eddy fluxes, *J. Phys. Oceanogr.*, **11**, 1677–1680, 1981.
- Mauritzen, C., Price, J., Sanford, T., and Torres, D.: Circulation and mixing in the Faroese Channels, *Deep-Sea Res. Pt. I*, **52**, 883–913, 2005.
- Müller, T. J., Meincke, J., and Becker, G. A.: Overflow’73: the distribution of water masses on the Greenland–Scotland ridge in August/September 1973; a data-report, *Institut für Meereskunde an der Christian-Albrechts-Universität Kiel*, 1967.
- Prater, M. D. and Rossby, T.: Observations of the Faroe Bank Channel overflow using bottom-following RAFOS floats, *Deep-Sea Res. Pt. II*, **52**, 481–494, 2005.
- Price, J. F. and O’Neil Baringer, M.: Outflow and deep water production by marginal seas, *Prog. Oceanogr.*, **33**, 161–200, 1994.
- Riemenschneider, U. and Legg, S.: Regional simulations of the Faroe Bank Channel overflow in a level model, *Ocean Model.*, **17**, 93–122, 2007.
- Saunders, P. M.: Cold outflow from the Faroe Bank Channel, *J. Phys. Oceanogr.*, **20**, 29–43, 1990.
- Saunders, P. M.: The dense northern overflows, in: *Ocean Circulation and Climate*, Chap. 5.6, edited by: Siedler, G., Church, J., and Gould, J., Academic Press, London, UK, 401–417, 2001.
- Seim, K. S., Fer, I., and Berntsen, J.: Regional simulations of the Faroe Bank Channel overflow using a  $\sigma$ -coordinate ocean model, *Ocean Model.*, **35**, 31–44, 2010.

- [Swift, J. H.: The circulation of the Denmark Strait and Iceland–Scotland overflow waters in the North Atlantic, \*Deep-Sea Res.\*, 31, 11, 1339–1355, 1984.](#)
- [Tait, J. B. \(ed.\): The Iceland–Faroe Ridge international \(ICES\) “Overflow” expedition, May–June, 1960, \*Rapp. PV Reun. Cons. Int. Explor. Mer.\*, 157, 1–274, 1967.](#)
- Thorpe, S. A.: An Introduction to Ocean Turbulence, Cambridge University Press, Cambridge, UK, 2007.
- Ullgren, J. E., Fer, I., Darelius, E., and Beird, N.: Interaction of the Faroe Bank Channel overflow with Iceland Basin intermediate waters, *J. Geophys. Res.-Oceans*, 119, 228–240, doi:10.1002/2013JC009437, 2014.
- van Aken, H. M.: The Oceanic Thermohaline Circulation. An Introduction, vol. 39 of Atmospheric and Oceanographic Sciences Library, Springer, New York, USA, 2007.
- van Aken, H. and Becker, G.: Hydrography and through-flow in the north-eastern North Atlantic Ocean: the NANSEN project, *Prog. Oceanogr.*, 38, 297–346, 1996.
- Voet, G. and Quadfasel, D.: Entrainment in the Denmark Strait overflow plume by meso-scale eddies, *Ocean Sci.*, 6, 301–310, doi:10.5194/os-6-301-2010, 2010.
- [Whitehead, J. A. and Worthington, L. V.: The flux and mixing rates of Antarctic bottom water within the North Atlantic, \*J. Geophys. Res.\*, 87, C10, 7903–7924, 1982.](#)

**Table A1.** Mooring positions, instrumentation, and data return. The nominal depth level of each instrument is given as height above bottom, HAB (m). Temperature is measured at every level, and any additional parameters measured are indicated as follows: conductivity as underlined, pressure as bold, and velocity in square brackets. The full deployment length was 372 days; any shorter records are marked by superscripts and the record length given in the column on the right. For current profilers, the target range is shown in a separate column. Instrument types are abbreviated as follows: SBE37 (s37), SBE39 (s39), SBE56 (s56), Continental (con), downward-looking RDI (rdD), upward-looking RDI (rdU), Aquadopp (aqd), RCM-7 (rm7), [Seaguard \(sea\)](#). Three of the short records (superscript 3, 6, and 9) are from the downward-looking RDI ADCPs at moorings C2, M1, and S3 respectively, that were set at a higher sampling resolution.

Mooring Depth (m)	Lon. (W) Lat. (N)	Target HAB (m) Instrument type	Velocity range (m)	Data days (if < 372)
C1 650	8°27.9' 61°40.4'	10, 30, 40, <b>50</b> , 60, 80, <u>100</u> , 125, <b>150</b> , 175 <sup>1</sup> , 200 <sup>2</sup> , <b>[202]</b> s56, s56, s56, s37, s56, s56, s37, s56, s39, s56, s37, con	20–195	<sup>1</sup> 204, <sup>2</sup> 152
C2 807	8°32.5' 61°37.4'	<b>25</b> , <b>[27]</b> , 50, 75, <u>100</u> , 125, <b>150</b> , 175, 200, <b>[200]</b> <sup>3</sup> , <b>250</b> , 300 <sup>4</sup> , 350, <b>[401]</b> s37, aqd, s56, s56, s37, s56, s39. s56, s56, rdD, s37, s56, s56, rdD	92–192 15–367	<sup>3</sup> 120, <sup>4</sup> 301
C3 859	8°37.7' 61°33.6'	<u>[25]</u> , <u>27</u> , <u>100</u> , <b>140</b> , <b>[150]</b> <sup>5</sup> rm7, s37, s37, s39, rdD	14–142	<sup>5</sup> 234
M1 808	9°20.0' 61°45.0'	<u>[25]</u> , <u>27</u> , 50, 75, <u>100</u> , <b>125</b> , 150, <u>170</u> , <b>[175]</b> <sup>6</sup> , 200, 250, <b>300</b> rm7, s37, s56, s56, s37, s39, s56, s37, rdD, s56, s56, s39	67–167	<sup>6</sup> 94
S1 610	9°29.0' 61°54.9'	<b>[80]</b> <sup>7</sup> rm7		<sup>7</sup> 371
S2 805	9°36.5' 61°49.2'	<b>[25]</b> <sup>8</sup> , <u>27</u> , 50, 75, <u>100</u> , <b>150</b> , 175, <b>200</b> , <b>250</b> , <b>[275]</b> rm7, s37, s56, s56, s37, s39, s56, s37, s39, rdD	34–258	<sup>8</sup> 371
S3 950	9°43.2' 61°43.6'	<u>[25]</u> , <u>27</u> , 50, <u>100</u> , 125, <b>150</b> , <b>[175]</b> <sup>9</sup> , 200, <b>250</b> , 300, 350, 400 <sup>10</sup> , 450, <b>500</b> <sup>11</sup> , <b>[502]</b> <sup>12</sup> , <b>[503]</b> rm7, s37, s56, s37, s56, s39, rdD, s56, s37, s56, s37, s56, s56, s56, s56, s37, rdD, rdU	67–167 20–486 520–816	<sup>9</sup> 109, <sup>10</sup> 326 <sup>11</sup> 328, <sup>12</sup> 281
S4 1082	9°49.1' 61°38.5'	<u>[25]</u> <sup>13</sup> , <u>27</u> , 50, <b>[75]</b> <sup>14</sup> , <b>100</b> , 125 <sup>14</sup> , <b>[150]</b> , <b>175</b> , 200 <sup>14</sup> , <b>250</b> , 299, <b>[300]</b> <sup>14</sup> rm7, s37, s56, rm7, s37, s39, sea, s39, s39, s37, s56, rm7		<sup>13</sup> 1 <sup>14</sup> 371

**Table A2.** Table showing maximum pulldown (from pressure sensors); percentage of time that pulldown is larger than 25, 50, or 100 m, respectively; ~~and~~ RMS error,  ~~$e$~~ , of the pulldown from the recorded pressure and modelled with MDD (Dewey, 1999); and the percent data discarded for each velocity recording instrument, listed from bottom upwards for each mooring, cf. table A1.

	HAB (m)	$\Delta H_{\max}$ (m)	$\Delta H > 25$ (%)	$\Delta H > 50$ (%)	$\Delta H > 100$ (%)	$e_{25}$ (m)	$e_{50}$ (m)	$e_{100}$ (m)	<u>Instr. discarded (%)</u>
C1	150	16	0	0	0	–	–	–	<u>con:0</u>
C2	250	100	7.96	1.54	0	10	16	36	<u>aqd:0, rdD:2.7, rdD:2.6</u>
C3	140	54	4.06	0.01	0	2	3	–	<u>rm7:0, rdD:0</u>
S2	250	118	3.97	1.23	0.09	12	15	20	<u>rm7:0.3, rdD:0</u>
S3	500	141	4.49	1.22	0.12	24	40	76	<u>rm7:0, rdD:2.3, rdD:2.4, rdU:0</u>
S4	250	48	0.18	0	0	15	–	–	<u>rm7:0, rm7:0, sea:0, rm7:0</u>

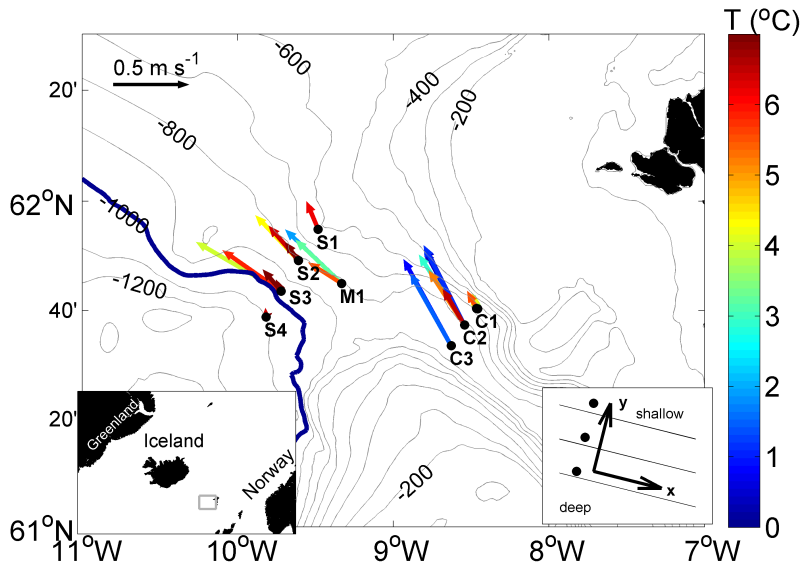


**Figure 1.** Map of the study region with the mooring positions (black dots) and mean current vectors from selected levels (75, 100, 150, 200, 250, and 300 m above the seabed) at each site, colour-coded by mean temperature from the same depth level (colour scale in °C on the right). Depth contours in grey are shown every 100 m with the 1000 m isobath bold, black. Insets show (left) the location of the study area and (right) the orientation of the coordinate system with respect to the mooring arrays.

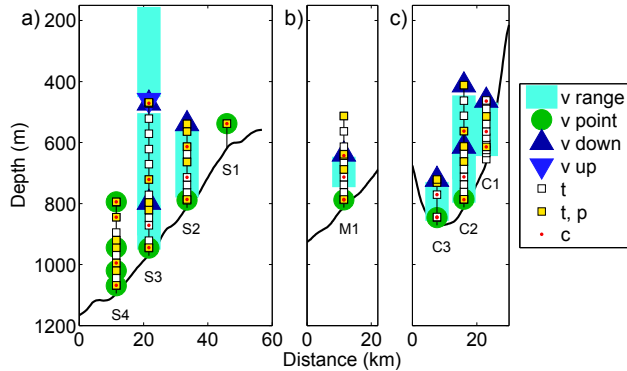


**Figure 2.** Mooring arrays: **(a)** section S, **(b)** mooring M1, and **(c)** section C. Each section is viewed looking downstream (southernmost mooring on the left). Sensors for temperature, pressure, conductivity, point velocity, as well as the range covered by the upward and downward oriented acoustic velocity profilers are indicated.

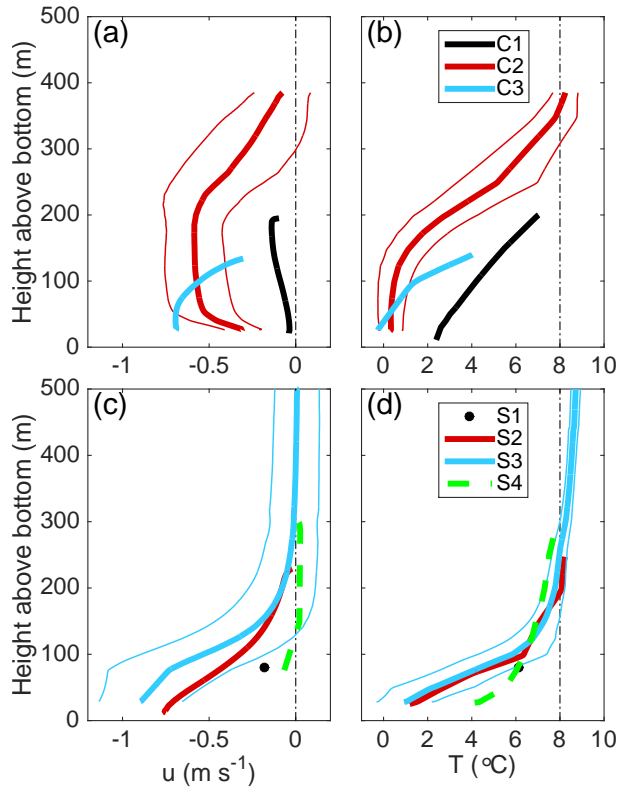


**Figure 3.** Mean vertical profiles of alongstream velocity  $u$  (left; **a**, **c**) and temperature (right; **b**, **d**) from the moorings in the C array (top; **a**, **b**) and the S array (bottom; **c**, **d**). Time-average profiles over the whole deployment are shown as bold lines, and one standard deviation from the mean as thin lines, shown for one mooring in each array (C2, S3). Thin black dash-dotted lines mark  $0 \text{ cm s}^{-1}$  and  $8 \text{ °C}$ , respectively. Only levels from which data are available at least 70% of the time are included.

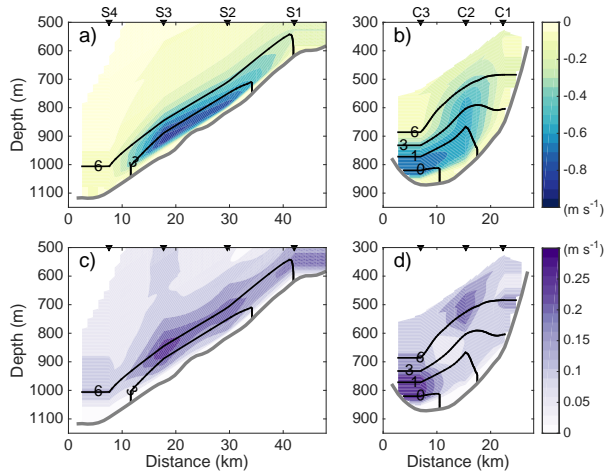


**Figure 4.** Cross-sectional distribution of alongstream velocity  $u$  ( $\text{m s}^{-1}$ ), in colour, with average isotherms ( $^{\circ}\text{C}$ ) overlaid as black contours. Time-average (**a**, **b**) and standard deviation (**c**, **d**) of daily data over the common period 29–30 May 2012–17 January 2013 when complete records exist at both sections: (**a**, **c**) section S, and (**b**, **d**) section C.

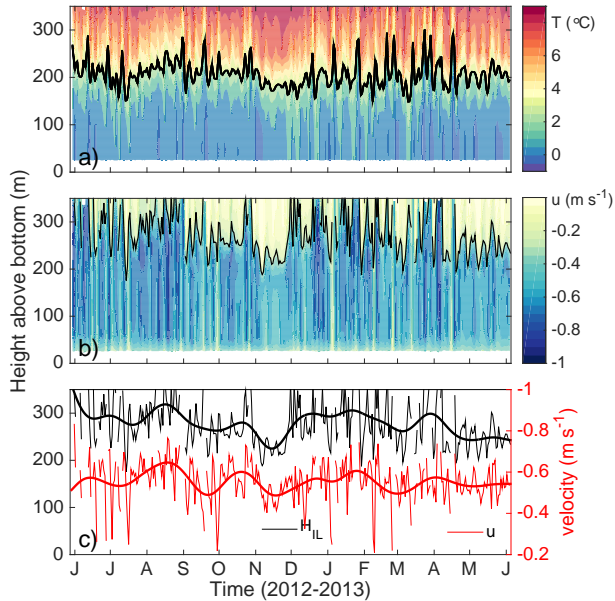


**Figure 5.** Time-height plots of daily **(a)** temperature ( $^{\circ}\text{C}$ ) and **(b)**  $u$  velocity ( $\text{m s}^{-1}$ ) from mooring C2. The bold black line in **(a)** marks the  $3^{\circ}\text{C}$  isotherm, and the thin black line in **(b)** is the kinematic interface height  $H_{IL}$ . **(c)** Time series of daily (thin) and 3 week low-passed (bold)  $H_{IL}$  (black) and the plume velocity (red) averaged within  $H_{IL}$ .

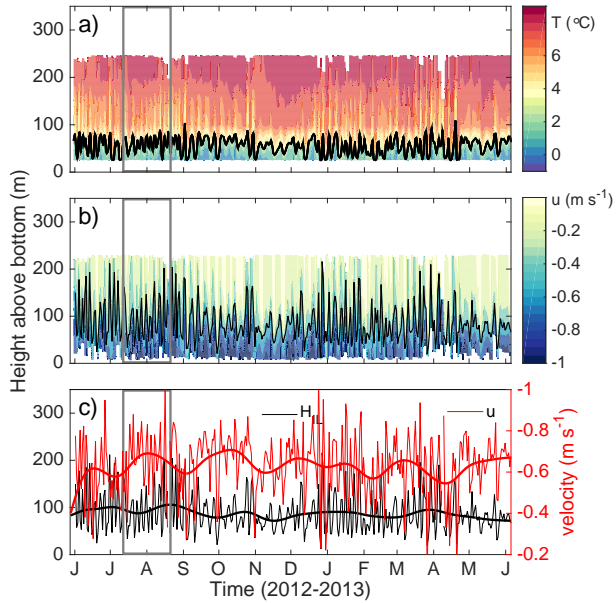


**Figure 6.** As Fig. 6-5 but for mooring S2. The grey boxes mark the time period shown in Fig. 11.

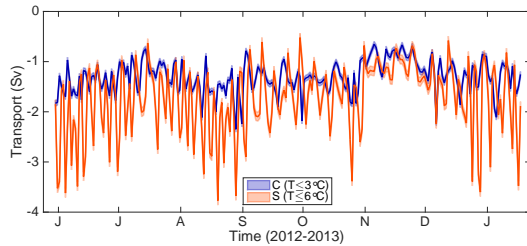


**Figure 7.** Time series of daily volume transport through mooring sections C (blue) and S (red). The transport at C includes water with temperature up to 3 °C and at S up to 6 °C. Shading shows the standard error for each time series.

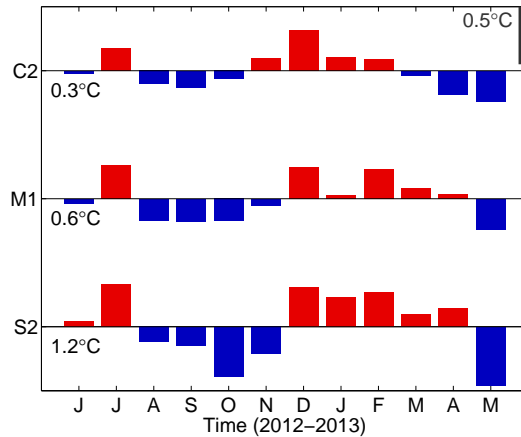


**Figure 8.** Time series of monthly mean temperature anomalies ( $^{\circ}\text{C}$ ) at [8025](#) mab from three moorings along the plume path (C2, M1, and S2; see labels on the left). Each series is shown as a fluctuation about the whole deployment mean, indicated by numbers below each axis (on the left). Scale bar is given in the top right corner.

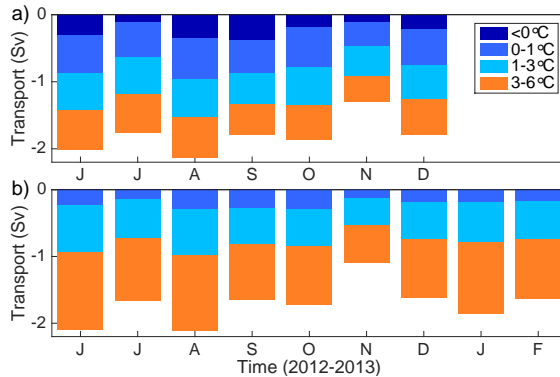


**Figure 9.** Monthly mean volume transport at **(a)** mooring array C, and **(b)** array S, per temperature class. The volume transport time series are shorter than a year because records from some current profilers (one at mooring C3 and one at mooring S3) did not cover the whole deployment, see Table A1.

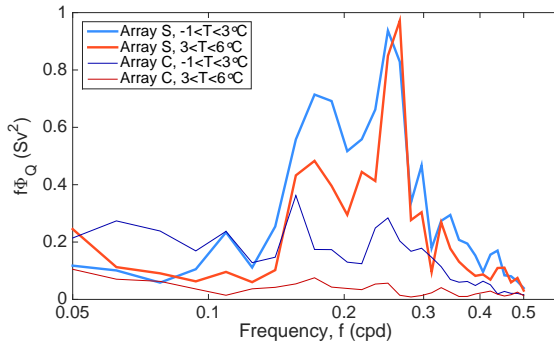


**Figure 10.** Variance preserving spectra of volume transport for the upper and lower layers at mooring arrays C and S, respectively.

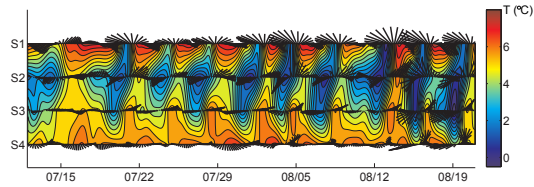


**Figure 11.** Hovmöller diagram of temperature ( $^{\circ}\text{C}$ ) and velocity anomalies at 80 mab across mooring section S. Temperature scale bar on right.

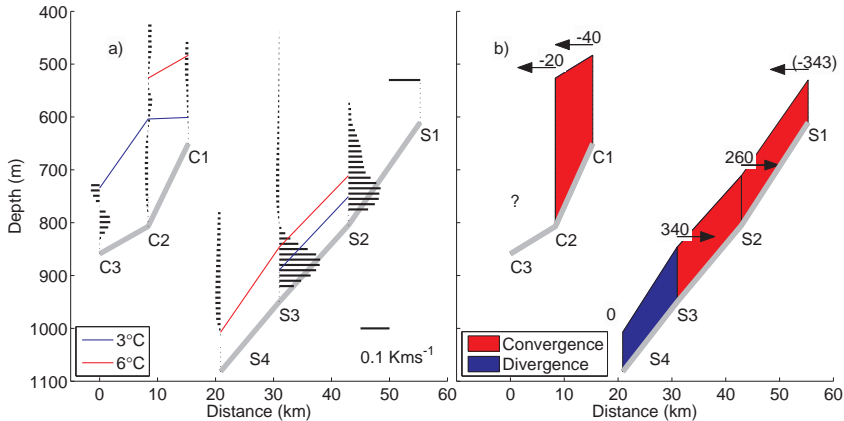


**Figure 12.** (a) Observed mean eddy temperature fluxes  $\overline{v'T'}$  at mooring array C and S (black bar) and the deployment mean position of the 3 °C (red-blue line) and 6 °C (blue-red line) isotherm. The bottom is shown in grey and the scale for the temperature fluxes is given in the lower right corner. (b) Net eddy heat flux (10<sup>5</sup> W m<sup>-1</sup>), integrated up to the deployment mean position of the 6 °C isotherm (blue-red line in a). The colors indicate convergence (red) and divergence (blue) and the arrows show the direction of the flux while the numbers above the moorings give the magnitude.

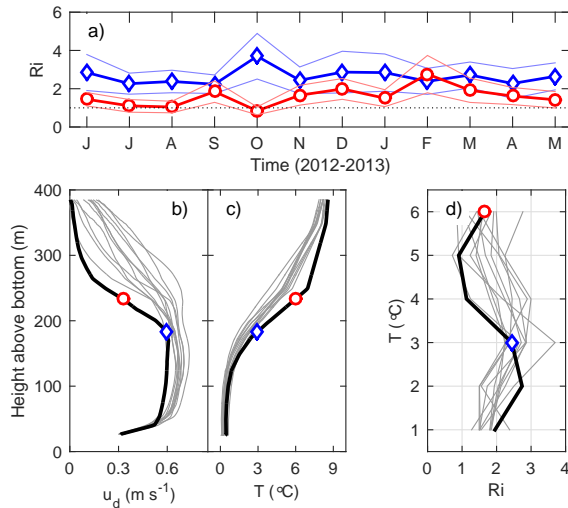


**Figure 13.** Monthly Richardson number,  $Ri$ , calculations at mooring C2 in the channel. **(a)** Monthly averages of hourly 10m  $Ri$  calculated at depths centered at the 3°C (blue, diamonds) and 6°C (red, circles) isotherms. Envelopes are the standard error assuming every 13th hourly sample is independent. Dashed line is  $Ri = 1$ . Profiles of **(b)** downstream velocity component and **(c)** temperature averaged in each month. The profile from May is highlighted by the bold line together with the depth of the 3 and 6°C isotherms by the corresponding markers. **(d)** Monthly 10m  $Ri$  for unit increment of  $T$ . The May profile is highlighted.

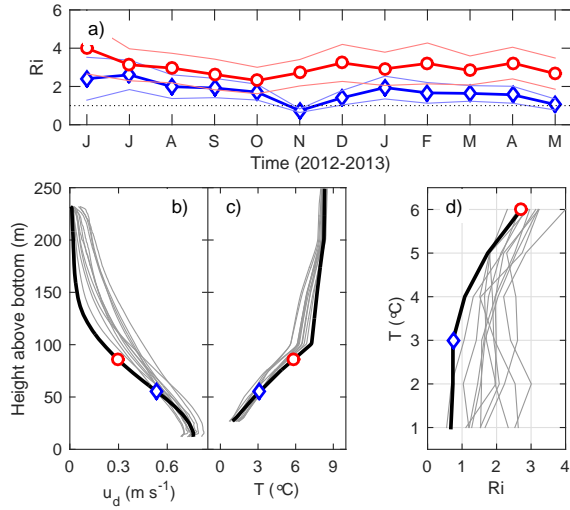


**Figure 14.** Same as Fig. 13, but for mooring S2, on the slope.

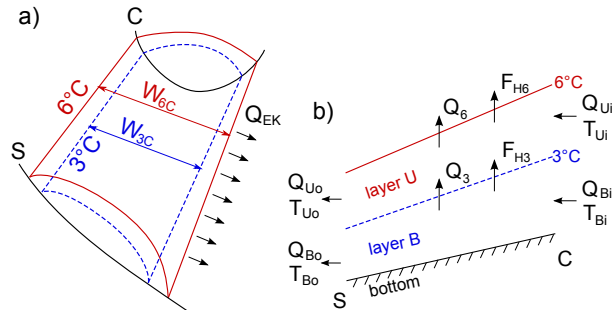


**Figure 15.** A schematic view of the overflow plume between sections C and S, demonstrating the components of the heat budget. The 3 °C isotherm marks the upper limit of the bottom (B) layer, and the 6 °C isotherm the upper limit of the upper (U) layer.

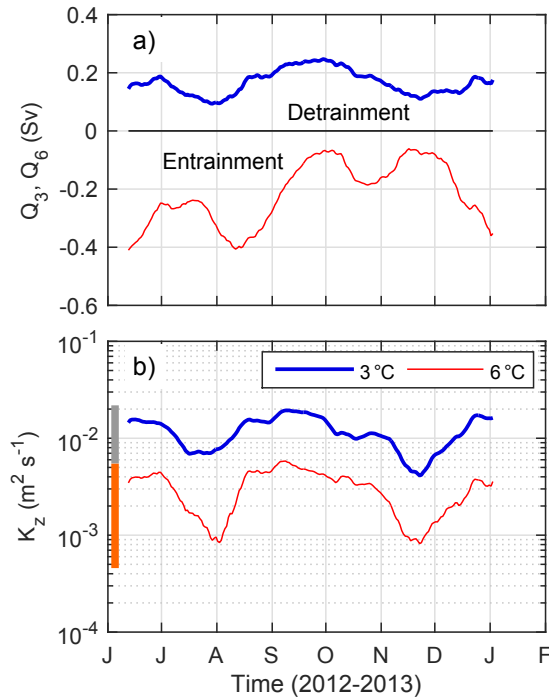


**Figure 16.** Time series of (a) detrainment and (b) vertical eddy diffusivity inferred from monthly heat budgets in daily moving windows. In (a) positive values indicate detrainment. Budgets are obtained between arrays C and S and between the bottom and the  $3^\circ C$  isotherm (blue) and between the 3 and  $6^\circ C$  isotherms (red), cf. Fig. 15. Vertical bars in (b) are the ranges of eddy vertical diffusivity in the corresponding layers, observed in June 2010 and 2012 using microstructure profilers (Fer et al., 2010, 2014).

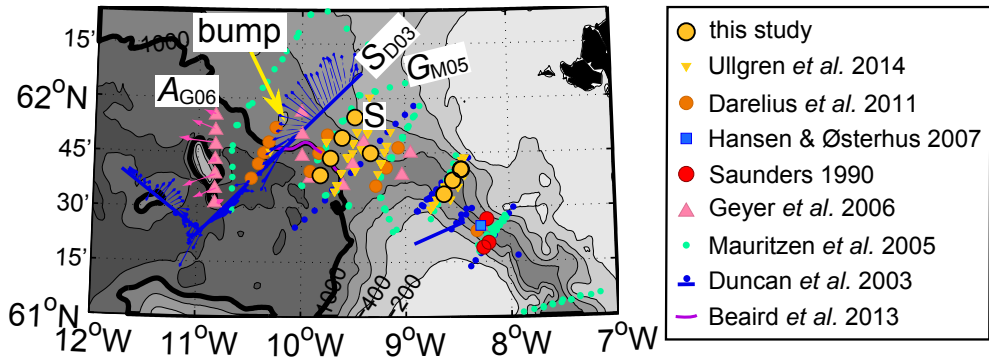


**Figure 17.** Map showing the positions of the moorings in this study together with the mooring positions of Darelius *et al.* (2011); Hansen and Østerhus (2007); Saunders (1990); Geyer *et al.* (2006). Also shown are CTD station positions from Ullgren *et al.* (2014) as well as station locations from Mauritzen *et al.* (2005), and hydrographic sections with CTD/LADCP and deep towed vehicle from Duncan *et al.* (2003). Shaded bathymetric contours are plotted every 200 m; the 1000 m contour is bold. Our mooring array S, Geyer's (2006) mooring array A ( $A_{G06}$ ), Duncan's section S ( $S_{D03}$ ), and Mauritzen's section G ( $G_{M05}$ ) are labelled. Current arrows from  $S_{D03}$  and  $A_{G06}$  are shown schematically, not to scale. The topographic bump associated with bifurcation of the flow is marked by a yellow arrow, and a purple line roughly corresponds to the portion of the 1000-m isobath where the deeper edge of the plume was found to be deeper than the depth range of Seagliders in Beaird *et al.* (2013) (see their figure 6).

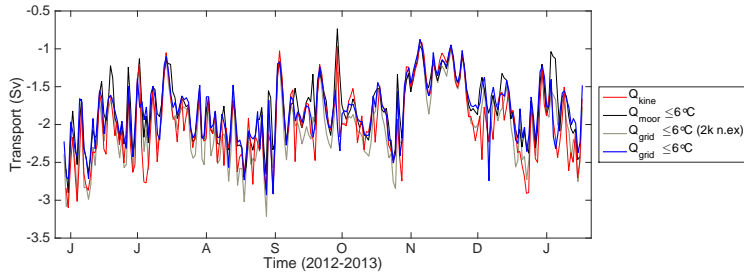


**Figure A1.** Time series of volume transport at mooring section C computed by different methods: kinematic ( $Q_{\text{kine}}$ ), per mooring ( $Q_{\text{moor}}$ ) and from gridded fields ( $Q_{\text{grid}}$ ). The latter two methods allow calculation of transport by temperature range, and results are shown here for the  $\leq 6^\circ\text{C}$  temperature class. The grey line represents a version with a 2 km horizontal grid and no upward extrapolation (which led to data from the longest, central mooring dominating the upper levels of the grid), and the blue line is the version used to produce the values of  $Q_{\text{grid}}$  reported in Sect. 4.